



HAL
open science

The FIGNL1-FIRRM complex is required to complete meiotic recombination in the mouse and prevents massive DNA damage-independent RAD51 and DMC1 loading

Akbar Zainu, Pauline Dupaigne, Soumya Bouchouika, Julien Cau, Julie Clément, Pauline Auffret, Virginie Ropars, Jean-Baptiste Charbonnier, Bernard de Massy, Rajeev Kumar, et al.

► To cite this version:

Akbar Zainu, Pauline Dupaigne, Soumya Bouchouika, Julien Cau, Julie Clément, et al.. The FIGNL1-FIRRM complex is required to complete meiotic recombination in the mouse and prevents massive DNA damage-independent RAD51 and DMC1 loading. 2023. hal-04237021

HAL Id: hal-04237021

<https://hal.science/hal-04237021v1>

Preprint submitted on 11 Oct 2023

HAL is a multi-disciplinary open access archive for the deposit and dissemination of scientific research documents, whether they are published or not. The documents may come from teaching and research institutions in France or abroad, or from public or private research centers.

L'archive ouverte pluridisciplinaire **HAL**, est destinée au dépôt et à la diffusion de documents scientifiques de niveau recherche, publiés ou non, émanant des établissements d'enseignement et de recherche français ou étrangers, des laboratoires publics ou privés.

1
2
3
4
5
6
7
8
9
10
11
12
13
14
15
16
17
18
19
20
21
22
23
24
25
26
27
28
29
30
31

The FIGNL1-FIRRM complex is required to complete meiotic recombination in the mouse and prevents massive DNA damage-independent RAD51 and DMC1 loading

Akbar Zainu¹, Pauline Dupaigne², Soumya Bouchouika^{1,3}, Julien Cau⁴, Julie A. J. Clément⁵, Pauline Auffret^{1,6}, Virginie Ropars⁷, Jean-Baptiste Charbonnier⁷, Bernard de Massy¹, Rajeev Kumar⁸, Frédéric Baudat⁹

¹ Institut de Génétique Humaine, University of Montpellier, CNRS, Montpellier, France.

² Genome Integrity and Cancers UMR9019 CNRS, Université Paris- Saclay, Gustave Roussy, F-94805 Villejuif Cedex, France.

³ Present address: Institut de Génétique Moléculaire de Montpellier, CNRS-UMR 5535, Univ Montpellier, Montpellier, France.

⁴ Biocampus Montpellier, University of Montpellier, CNRS, INSERM, Montpellier, France

⁵ IHPE, Univ Montpellier, CNRS, IFREMER, Univ Perpignan Via Domitia, Perpignan, France

⁶ Present address: Ifremer, IRSI, Service de Bioinformatique (SeBiMER), Plouzané, France.

⁷ Institute for Integrative Biology of the Cell (I2BC), Université Paris-Saclay, CEA, CNRS, Gif-sur-Yvette, France.

⁸ Institut Jean-Pierre Bourgin, INRA, AgroParisTech, CNRS, Université Paris-Saclay, 78000 Versailles, France.

⁹ Institut de Génétique Humaine, University of Montpellier, CNRS, Montpellier, France.

frederic.baudat@igh.cnrs.fr

Running title: FIGNL1-FIRRM in mouse meiosis

Keywords: meiosis; homologous recombination; FIGNL1; FIRRM; RAD51; DMC1

32 **Abstract**

33

34 During meiosis, nucleoprotein filaments of the strand exchange proteins RAD51 and DMC1 are crucial
35 for repairing SPO11-generated DNA double-strand breaks (DSBs) by homologous recombination (HR).
36 A balanced activity of positive and negative RAD51/DMC1 regulators ensures proper recombination.
37 Fidgetin-like 1 (FIGNL1) was previously shown to negatively regulates RAD51 in human cells. However,
38 FIGNL1's role during meiotic recombination in mammals remains unknown. Here, we deciphered the
39 meiotic functions of FIGNL1 and of FIGNL1 interacting regulator of recombination and mitosis (FIRRM)
40 using male germline-specific conditional knock-out (cKO) mouse models. Both FIGNL1 and FIRRM are
41 required for completing meiotic prophase in mouse spermatocytes. Despite efficient recruitment of
42 DMC1 on ssDNA at meiotic DSB hotspots, the formation of late recombination intermediates is
43 defective in *Firrm* cKO and *Fignl1* cKO spermatocytes. Moreover, the FIGNL1-FIRRM complex limits
44 RAD51 and DMC1 accumulation on intact chromatin, independently from the formation of SPO11-
45 catalyzed DSBs. Purified human FIGNL1 Δ N alters the RAD51/DMC1 nucleoprotein filament structure
46 and inhibits strand invasion *in vitro*. Thus, this complex might regulate RAD51 and DMC1 association
47 at sites of meiotic DSBs to promote proficient strand invasion and processing of recombination
48 intermediates.

49

50 **Introduction**

51

52 Meiosis ensures the accurate reduction of chromosome numbers in gametes during sexual
53 reproduction. Erroneous meiosis results in sterility or fertility defects owing to aberrant gametes
54 formation. During meiosis, homologous chromosomes (homologs) undergo pairing, synapsis, and
55 recombination. Homologous recombination (HR) is crucial for crossover (CO) formation between
56 homologs to ensure their balanced segregation during meiosis, and for promoting pairing and synapsis
57 of homologs in some organisms including mammals¹⁻³. HR is initiated by genome-wide SPO11-
58 dependent DNA double-strand breaks (DSBs) formation⁴. SPO11 is subsequently released from DSB
59 sites as SPO11-oligonucleotide complex by resection machinery giving rise to 3' single-stranded DNA
60 (ssDNA) overhangs^{5,6}. The heterotrimeric complex of Replication Protein A (RPA) binds to and protects
61 the ssDNA overhangs from nucleolytic degradation. Two eukaryotic RecA-like strand-exchange
62 proteins, RAD51 and its meiosis-specific paralog DMC1, replace RPA on ssDNA with the help of the
63 mediator protein BRCA2^{7,8}. Both strand exchange proteins can catalyze homology search and strand
64 exchange through invasion on an intact template, leading to formation of a joint molecule termed

65 displacement loop (D-loop)⁹. The invading end primes DNA synthesis that requires the dissociation of
66 RAD51/DMC1 from double-strand DNA (dsDNA) within the D-loop. After D-loop formation, meiotic
67 DSB repair can produce a non-crossover (NCO), or a CO by two alternative pathways that coexist in
68 many organisms². In mice, the meiosis-specific class I CO pathway generates 90% of COs and is
69 dependent on a set of proteins referred to as ZMM proteins (including the MSH4-MSH5 complex and
70 TEX11)^{10,11} and the MutL homologs MLH1-MLH3. Mouse MSH4 and MSH5 are essential to repair most
71 if not all meiotic DSBs^{2,12-14}. The class II COs (~10% of COs in the mouse) depend on structure-specific
72 endonucleases².

73 Both RAD51 and DMC1 form foci colocalizing extensively at DSB sites^{15,16} and are proposed to
74 assemble into side-by-side homo-filaments on ssDNA tails, with RAD51 at the DSB-distal region and
75 DMC1 polymerizing on the 3', DSB-proximal region^{9,17,18}. DMC1 is likely the main catalyzer of meiotic
76 interhomolog recombination in most eukaryotes, while RAD51 plays crucial non-catalytic accessory
77 roles¹⁸⁻²⁰. RAD51 is the sole strand exchange protein during mitotic recombination and also plays a
78 strand exchange activity-independent role in the replication fork protection that might rely on its
79 dsDNA-binding capacity²¹⁻²⁶. Besides this specific function, inactive filaments of RAD51 and DMC1 on
80 dsDNA are likely toxic and are actively prevented²⁷. Members of the Swi2/Snf2-related RAD54
81 translocase family²⁸ prevent the accumulation of RAD51 on dsDNA in human cells²⁹, and of Rad51 and
82 Dmc1 in *S. cerevisiae*^{30,31}. In *S. cerevisiae*, Rad54 and its paralog Rdh54 promote strand invasion, and
83 remove RAD51/DMC1 from dsDNA following D-loop formation^{28,32}. In mouse, RAD54 and its paralog
84 RAD54B are not essential for meiotic recombination, because the *Rad54 Rad54b* double mutant mice
85 are fertile^{33,34}. Many proteins regulate RAD51/DMC1 nucleofilament formation positively and
86 negatively. Positive factors are required to form stable and active RAD51-ssDNA filaments^{7,8}. One of
87 them is the Shu complex that comprises in mammals the distant RAD51 paralog SWSAP1, the SWIM-
88 domain containing SWS1 and SPIDR³⁵⁻³⁹. It promotes the formation of stable RAD51 filaments and HR
89 associated with replication, is important for assembling stable RAD51 and DMC1 filaments during
90 meiotic recombination in the mouse, but is not essential for viability^{36,37,40-42}. The SWSAP1-SWS1-
91 SPIDR complex might promote specifically the stable assembly of longer RAD51 nucleoprotein
92 filaments involved in some HR types, especially interhomolog HR^{36,37}.

93 FIGNL1 (fidgetin-like 1) forms an evolutionary conserved complex with FIRRM (FIGNL1 interacting
94 regulator of recombination and mitosis) that interacts with RAD51 and DMC1⁴³⁻⁴⁶. In Arabidopsis and
95 rice meiosis, FIGNL1 and FIRRM homologs regulate negatively the dynamics of RAD51 and DMC1 foci
96 and limit the formation of class II crossovers^{44,45,47-49}. Arabidopsis *figl1* (*Figl1* homolog) and *flip* (*Firrm*
97 homolog) mutants are fertile with all meiotic DSBs repaired^{44,47,50}. Conversely, unrepaired DSBs persist
98 in rice *fignl1* and *meica* (*Firrm* homolog) mutants, leading to chromosome fragmentation and sterility
99^{48,49}. The regulation of RAD51/DMC1 focus formation in Arabidopsis somatic and meiotic cells involves

100 an antagonistic interplay between BRCA2 and FIGL1, consistent with FIGL1 acting as a negative
101 regulator of RAD51/DMC1 filament⁵¹. In human cells, a similar antagonistic mechanism was found
102 between the SWSAP1-SWS1-SPIDR complex and FIGNL1, which interacts with SWSAP1⁴¹ and SPIDR⁴³.
103 Indeed, FIGNL1 depletion relieves the dependency on SWSAP1 and SWS1 for forming RAD51 repair
104 foci⁴¹. Moreover, purified human SWSAP1 protects RAD51-ssDNA filament from dissociation
105 promoted by FIGNL1 *in vitro*⁴¹. However, the role of FIGNL1 and FIRRM remains unknown during
106 meiotic recombination in mammals.

107

108 In this study, we investigated the role of the FIGNL1-FIRRM complex in meiotic recombination by
109 analyzing germ line-specific mouse conditional knock-out models for both genes. The depletion of
110 FIGNL1 or FIRRM in mouse spermatocytes results in meiotic DSB repair failure and no full synapsis
111 between homologs during meiotic prophase I, leading to prophase I arrest and apoptosis. Surprisingly,
112 *Figl1* cKO and *Firrm* cKO spermatocytes also show an abundant DSB-independent accumulation of
113 RAD51 and DMC1 on chromatin and meiotic chromosome axes during premeiotic replication and early
114 meiotic prophase stages. This indicates that the FIGNL1-FIRRM complex prevents the formation of
115 stable inactive RAD51 and DMC1 filament, presumably on intact dsDNA, in mouse spermatocyte nuclei.

116

117

118 **Results**

119

120 **FIGNL1 and FIRRM are required for meiotic prophase completion in the mouse male germline**

121 We wanted to determine the roles of FIGNL1 and its putative partner FIRRM (also called BC055324)
122 during meiosis. As both genes are essential for mouse viability (IMPC,
123 <https://www.mousephenotype.org/>), we generated cKO lines with Cre expression under the control
124 of the *Stra8* promoter⁵² to ablate *Firrm* or/and *Figl1* in the male germline shortly before meiosis
125 onset (*Firrm* cKO and *Figl1* cKO, Extended Data Fig. 1a-b). Testis weight was similarly reduced in *Firrm*
126 cKO, *Figl1* cKO, and *Firrm-Figl1* double cKO mice compared with wild-type controls (Fig. 1a). Analysis
127 of testis sections from adult *Firrm* cKO and *Figl1* cKO animals showed the presence of seminiferous
128 tubules with Sertoli cells, spermatogonia and spermatocytes, but absence of haploid cells (spermatids),
129 suggesting a prophase I arrest (Fig. 1b). The presence of some tubules with a small number of round
130 spermatids and of few tubules with many round and elongated spermatids, like in controls, suggested
131 incomplete Cre-mediated excision, as described in other conditional mouse mutants obtained with this
132 *Stra8-Cre* transgene⁵³⁻⁵⁵. In testes from 12-day post-partum (12 dpp) *Firrm* cKO and *Figl1* cKO mice,
133 FIRRM and FIGNL1 protein expression levels in the cytoplasmic and nuclear fractions were greatly and

134 similarly reduced compared to controls (Fig. 1c). This suggests that they reciprocally regulate their
135 stability, which is consistent with forming a complex. The residual protein level might result from
136 expression in non-meiotic cells (spermatogonia or somatic cells) and/or from incomplete Cre-induced
137 gene deletion in a fraction of spermatocytes (see above). Conversely, RAD51 expression in the nuclear
138 fraction was increased in *Firrm* cKO and *Figl1* cKO testes, suggesting that the FIGNL1-FIRRM complex
139 might be implicated in limiting directly or indirectly nuclear accumulation of RAD51 (but not of DMC1).
140 This might have significant consequences, because RAD51 nuclear level is suggested play a role in HR
141 regulation ⁵⁶.

142
143 The synaptonemal complex (SC), a tripartite proteinaceous structure, links the axes of homologous
144 chromosomes during meiotic prophase. To analyze if synapsis was impaired in *Firrm* cKO and *Figl1*
145 cKO, we stained surface-spread spermatocyte nuclei with antibodies against SYCP3, a component of
146 meiotic chromosome axes, and SYCP1, a protein of the SC central element (Fig. 1d). *Firrm* cKO and
147 *Figl1* cKO spermatocytes formed apparently normal meiotic chromosome axes (leptotene stage),
148 suggesting a normal meiotic prophase entry. However, most nuclei showed unsynapsed or partially
149 synapsed axes, indicating accumulation of zygotene-like cells. The small fraction of *Figl1* cKO and
150 *Firrm* cKO spermatocytes that progressed toward normal-looking pachytene with all chromosomes
151 pairs fully synapsed and diplotene with desynapsed chromosomes might be explained by incomplete
152 Cre-mediated excision in these cells (Fig. 1e). We followed prophase I progression during the first wave
153 of meiosis in *Firrm* cKO, from 12 dpp to 18 dpp. We detected a deficit in more advanced stages already
154 in 12 dpp *Firrm* cKO spermatocytes. At 16 and 18 dpp, most nuclei were arrested at a zygotene-like
155 stage, and the percentage of nuclei at the pachytene and diplotene stages was strongly reduced (at 18
156 dpp, 78% of control versus 15% of *Firrm* cKO nuclei). Approximately 30% of *Firrm* cKO prophase I nuclei
157 displayed an abnormal zygotene/pachytene-like pattern, with non-homologous synapsis and only few
158 synapsed chromosome axes (Fig. 1d, middle panel). These findings in 12 dpp to 18 dpp spermatocytes
159 are suggestive of an arrest in early pachytene and a defect in homologous synapsis. Adult *Figl1* cKO
160 animals displayed a similar deficit in pachytene-diplotene spermatocytes (Fig. 1e), consistent with the
161 hypothesis that FIGNL1 and FIRRM act together.

162 163 **The formation and initial processing of meiotic DSBs are unaffected in *Firrm* cKO and *Figl1* cKO** 164 **spermatocytes**

165 This synapsis defect associated with a mid-prophase arrest might result from defective recombination
166 initiation (e.g. *Spo11*^{-/-} ^{57,58}) or defective repair of meiotic DSBs (e.g. *Dmc1*^{-/-} ^{59,60}) ³. To determine
167 whether DSB formation was altered by FIRRM or FIGNL1 depletion, we quantified phosphorylated
168 H2AX (γ H2AX) that decorates chromatin in a DSB-specific manner at leptotene ⁶¹. The γ H2AX signal

169 intensity in the nucleus was not different in control and *Firrm* cKO spermatocytes from pre-leptotene
170 (stage of pre-meiotic replication) to leptotene (Fig. 2a-b). RPA2, a subunit of RPA, is involved in DNA
171 replication and HR and forms multiple foci at replication forks in preleptotene spermatocytes, and
172 along chromosome axes at sites of recombination intermediates from leptotene to pachynema^{53,62,63}.
173 RPA2 foci displayed the same kinetics in *Firrm* cKO, *Figl1* cKO, and control spermatocytes (Fig. 2c-d),
174 except for a trend toward an increase in early zygonema (by 1.3- and 1.4-fold for *Firrm* cKO and *Figl1*
175 cKO, respectively). Thus, the first steps of meiotic recombination (DSB formation and RPA recruitment
176 on resected ssDNA ends) were not affected by the absence of the FIGNL1-FIRRM complex.

177

178 **The recruitment of RAD51 and DMC1 on meiotic chromatin strongly increases in the absence of** 179 **FIGNL1 or FIRRM**

180 In mouse spermatocytes, RAD51 and DMC1 foci extensively colocalize on meiotic chromosome axes
181 (on-axis foci) from leptotene to pachytene stage, particularly in zygotene^{15,16,62}. Compared with
182 controls, RAD51 and DMC1 signal intensity and foci pattern and kinetics were strikingly different in
183 *Firrm* cKO and *Figl1* cKO spermatocytes (Fig. 3a-c; Extended Data Fig. 2a). First, RAD51 (but not DMC1)
184 formed many foci at preleptotene, during premeiotic replication. Second, the mean number of RAD51
185 and DMC1 on-axis foci was significantly higher in *Firrm* cKO and *Figl1* cKO than in control
186 spermatocytes at every stage, from early leptotene to zygotene. Third, in cKO spermatocytes, many
187 RAD51 and DMC1 foci were located away from the chromosome axes (off-axis foci). The number of
188 off-axis foci was highest during leptotene and progressively decreased during zygotene. Fourth, in cKO
189 spermatocytes, RAD51 and DMC1 staining formed continuous lines, at our resolution limit, along the
190 synaptonemal complex segments in zygotene-like nuclei. This did not allow counting RAD51 and DMC1
191 foci in late zygotene-like nuclei with extensive synapsis. Overall, these observations are consistent with
192 a role of FIRRM and FIGNL1 in limiting RAD51 and DMC1 loading on chromatin in spermatocyte nuclei.
193 We describe these different features in the following sections.

194

195 **Post-strand invasion recombination foci are strongly reduced in the absence of FIRRM**

196 The efficient recruitment of RAD51 and DMC1 prompted us to examine MSH4 and TEX11, two meiotic
197 stabilizing post-strand invasion recombination intermediate ZMM proteins¹¹, which form foci on SC
198 from zygotene to mid-pachytene^{3,62,64}. The number of MSH4 and TEX11 foci was strongly reduced in
199 late zygotene-like *Firrm* cKO nuclei compared with control (Fig. 3d, Extended Data Fig. 2b). To
200 normalize differences in SC extension among genotypes, we measured the density of MSH4 foci per
201 μm of SC length. MSH4 focus density was reduced by 2.5-fold in *Firrm* cKO compared with control
202 spermatocytes (Fig. 3e, Extended Data Fig. 2c), although the number of MSH4 foci was higher than in
203 *Spo11*^{YF/YF} nuclei (without DSB-inducing activity). Thus, FIRRM is required for TEX11 and MSH4 focus

204 formation during mouse meiotic recombination. The residual MSH4 foci might result from MSH4
205 binding to a small fraction of normal or aberrant recombination intermediates formed in the absence
206 of the FIGNL1-FIRRM complex. Alternatively, we cannot exclude the persistence of a small amount of
207 FIRRM protein in *Firrm* cKO spermatocytes, sufficient for recruiting MSH4 to few recombination
208 intermediates. Thus, despite the increased recruitment of RAD51 and DMC1 on chromosome axes, the
209 processing of recombination intermediates was defective in *Firrm* cKO spermatocytes, suggesting a
210 function of FIGNL1-FIRRM at a step likely before recombination intermediate stabilization by MSH4-
211 MSH5.

212

213 **In *Firrm* cKO and *Figl1* cKO preleptotene spermatocytes, RAD51 is recruited on chromatin during**
214 **premeiotic replication**

215 RPA2 forms many foci at ongoing replication forks in preleptotene nuclei (Fig. 3f-g). The kinetics of
216 RPA2 focus formation was similar in control, *Firrm* cKO and *Figl1* cKO spermatocytes, and few foci
217 remained in early leptotene stage. This suggests that premeiotic replication was completed without
218 major alteration (Fig. 2d; Extended Data Fig. 2d). As RAD51 is involved in protecting stalled replication
219 forks⁶⁵, we hypothesized that RAD51 might colocalize with RPA during premeiotic replication in *Firrm*
220 cKO and *Figl1* cKO spermatocytes. We measured the colocalization of RAD51 and RPA2 in
221 preleptotene spermatocytes and compared these data with the colocalization of randomly distributed
222 foci obtained from simulations (see Methods; Fig. 3h-i; Extended Data Fig. 2e). In *Figl1* cKO, 17% of
223 RAD51 foci colocalized with RPA2 foci compared with 9% of randomly generated RAD51 foci (p
224 <0.0001 ; two-tailed Wilcoxon test), suggesting that a fraction of RAD51 foci localizes at replication
225 forks. However, the majority of identified RAD51 foci was not coincided with RPA2 foci, suggesting that
226 a larger fraction of RAD51 foci may not localize at replication forks. We cannot exclude that both RAD51
227 and RPA localize at forks in an exclusive manner, and that RAD51 binding excludes RPA. However,
228 because of the large number of RAD51 foci that persisted at the end of premeiotic replication and the
229 absence of obvious gross replication defects, we hypothesize that RAD51 colocalizes transiently with
230 RPA at replication forks. It then remains in place, likely on intact DNA, while the forks progress and
231 move away. DMC1 foci were rare in most *Firrm* cKO and *Figl1* cKO preleptotene spermatocytes (Fig.
232 3c), likely because meiosis-specific DMC1 production is still low at preleptotene stage.

233

234 In meiosis, RAD51 and DMC1 colocalization throughout the meiotic prophase reflects their
235 cooperation at resected DSB ends^{15–18,66}. In *Firrm* cKO and *Figl1* cKO, RAD51 foci started to form
236 earlier and their number was higher in early leptotene compared with DMC1 foci (Fig. 3b-c). We
237 examined the colocalization of on-axis RAD51 and DMC1 foci from early leptotene (in *Firrm* cKO) and
238 leptotene (in control) to mid-zygotene stage, in nuclei containing at least 10 foci for each protein (Fig.

239 4a-c; Extended Data Fig. 3a). As expected, on-axis RAD51 foci, the number of which was higher,
240 colocalized less frequently with DMC1 foci in *Firrm* cKO than in control spermatocytes, especially at
241 earlier stages (Fig. 4b). Conversely, more or similar percentages of on-axis DMC1 foci colocalized with
242 on-axis RD51 foci in *Firrm* cKO and control spermatocytes at every stage, with a maximum in early
243 leptotene (~70%). Off-axis foci in *Firrm* cKO displayed the same trend, with a very high percentage of
244 DMC1 foci that colocalized with RAD51 foci at earlier stages (Extended Data Fig. 3b-e). Altogether,
245 these observations indicate that in the absence of FIRRM, off-and on-axis RAD51 foci assemble
246 independently of DMC1 foci in preleptotene and early prophase spermatocytes. Moreover, detectable
247 DMC1 foci might form by joining pre-existing RAD51 foci, or by co-assembling *de novo* RAD51-DMC1
248 foci in *Firrm* cKO spermatocytes.

249

250 **RAD51 and DMC1 form parallel linear structures along the synaptonemal complex in the absence of** 251 **FIRRM**

252 To refine the characterization of RAD51 and DMC1 distribution in *Firrm* cKO spermatocytes, we
253 visualized RAD51, DMC1 and SYCP3 using super-resolution stimulated emission depletion (STED)
254 microscopy (Fig. 4d-e). In leptotene and zygotene control spermatocytes, RAD51 and DMC1 formed
255 partially overlapping co-foci along the unsynapsed axes and SC segments. RAD51 was more often
256 closer to the chromosome axis than DMC1, as described previously^{18,66}. In *Firrm* cKO spermatocytes,
257 the patterns of RAD51 and DMC1 staining were more heterogeneous. A first type of RAD51-DMC1 co-
258 foci was similar to control foci, but RAD51 signal tended to be more extended compared with DMC1
259 (Fig. 4d, compare control insets with the two upper panels of *Firrm* cKO insets). Second, some co-foci
260 formed longer structures anchored to the chromosome axis, a pattern expected if they were extending
261 along chromatin fibers (middle panels of the inset). Thus, the localization patterns of these two types
262 of foci are compatible with RAD51/DMC1 filaments bound to chromatin fibers at DSB sites or/and
263 dsDNA. In addition, at some sites, RAD51 and DMC1 followed the unsynapsed axes, often filling gaps
264 with little or no SYCP3 signal between more heavily SYCP3-stained axis segments (bottom panels of
265 the insets). Lastly, in *Firrm* cKO zygotene-like nuclei with some synapses, RAD51 and DMC1 formed
266 two parallel lines separated by ~100 nm along SC segments, between the lateral elements (axes)
267 visualized by ~210 nm apart SYCP3 signal (Fig. 4e-f). The intensity of these lines was irregular with
268 interruptions, and interspersed with more intense foci. These observations suggest a highly aberrant
269 patterning of RAD51 and DMC1 on meiotic chromatin and on meiotic chromosome axes in the absence
270 of FIGNL1 and FIRRM activity.

271

272 **Accumulation of RAD51 and DMC1 foci in *Firrm* cKO spermatocytes is meiotic DSB-independent**

273 In *Firrm* cKO and *Figl1* cKO spermatocytes, RAD51 and DMC1 displayed an unusual pattern that
274 included an increased number of foci, many off-axis foci, and linear staining along chromosome axes.
275 This was different from the expected discrete DSB repair foci on chromosome axes^{16,62}, raising the
276 question of whether in these cKO models, RAD51 and DMC1 recruitment requires SPO11-generated
277 DSBs. Thus, we generated *Spo11^{YF/YF} Firrm* cKO double mutants in which SPO11 is catalytically dead⁶⁷.
278 The low early prophase γ H2AX staining and the absence of RPA2 foci confirmed the absence of DSBs
279 in these animals (Extended Data Fig. 4a-b). Strikingly, we detected large numbers of on-axis and off-
280 axis RAD51 and DMC1 foci in *Firrm* cKO and in *Spo11^{YF/YF} Firrm* cKO spermatocytes, and only
281 background signal in *Spo11^{YF/YF}* spermatocytes (as expected) (Fig. 5a). Overall, the pattern of RAD51
282 and DMC1 in *Firrm* cKO and *Spo11^{YF/YF} Firrm* cKO were similar: a large number of on-axis foci detected
283 from early prophase that persisted through zygotene, RAD51 foci formed during preleptotene stage,
284 and both RAD51 and DMC1 off-axis foci progressively disappeared from leptotene to zygotene (Fig.
285 5b-c; Extended Data Fig. 5a-b). Moreover, RAD51 and DMC1 association, measured as the
286 colocalization of on-axis foci, was similar in *Firrm* cKO and *Spo11^{YF/YF} Firrm* cKO, indicating that their
287 association is DNA damage-independent (Extended Data Fig. 5c-f).

288

289 **DMC1 is recruited to DSB sites in the absence of the FIGNL1-FIRRM complex**

290 The abundance of DSB-independent RAD51 and DMC1 foci raises the question of whether there is any
291 recruitment at meiotic DSB sites in the absence of FIRRM or FIGNL1. Therefore, we determined the
292 colocalization of on-axis DMC1 and RPA2 foci, used as a marker of a subset of the DSBs, in *Firrm* cKO
293 and *Figl1* cKO spermatocytes. The number of on-axis DMC1-RPA2 co-foci (corrected for random
294 colocalization) in spermatocytes followed the kinetics of RPA2 foci in all genotypes (Extended Data Fig.
295 6a-d, compare with Fig. 2d). In *Firrm* cKO and *Figl1* cKO spermatocytes, the percentage of on-axis
296 RPA2 foci that colocalized with DMC1 was similar to control spermatocytes in leptotene and tended to
297 be higher in mid-zygotene, possibly indicative of the accumulation of unrepaired HR intermediates (Fig.
298 6a; Extended Data Fig. 6e). The lower percentage of on-axis DMC1 foci that colocalized with RPA2 in
299 cKO spermatocytes compared with control might be explained by the excess of DSB-independent
300 DMC1 foci (Fig. 6b; Extended Data Fig. 6f). We obtained similar results also for on-axis RPA2-RAD51
301 co-foci in *Figl1* cKO (Fig. 7e; Extended Data Fig. 8d). These findings suggest that the efficiency of
302 RAD51 and DMC1 recruitment at sites of meiotic DSBs is not affected by FIRRM and FIGNL1 absence.

303

304 To assess directly DMC1 recruitment at SPO11-dependent DSB hotspots, we investigated the genome-
305 wide distribution of DMC1-bound ssDNA by chromatin-immunoprecipitation (ChIP), followed by ssDNA
306 enrichment (DMC1-Single Strand DNA Sequencing, SSSS)⁶⁸ in testes from 12-dpp control and *Firrm*
307 cKO mice. In control mice, the regions enriched in DMC1-bound ssDNA are the ssDNA 3'overhangs that

308 result from DSB resection at meiotic DSB hotspots⁶⁹. We detected 9,907 peaks in control and 7,397
309 peaks in *Firrm* cKO spermatocytes (Fig. 6c). Most of these peaks (6,614) were shared. Peaks called
310 specifically in one genotype or the other were most likely shared weakly active hotspots, as inferred
311 from their weak enrichment in both genotypes (Extended Data Fig. 7b). Most of the detected DMC1-
312 SSDS peaks (9,297 out of 10,690) overlapped with previously identified meiotic SPO11-oligonucleotide
313 DSB hotspots (SPO11-oligo hotspots, Extended Data Fig. 7a)⁷⁰. Moreover, the DMC1-SSDS signal
314 enrichment within peaks was highly correlated in control and *Firrm* cKO samples (Spearman's
315 $\rho=0.92$; Fig. 6d) with the exception of X chromosome hotspots, which were relatively less enriched
316 in *Firrm* cKO than in control samples (Extended Data Fig. 7d). One possible explanation for this could
317 be a genome-wide accumulation of HR intermediates in *Firrm* cKO that would erase the X
318 chromosome-specific higher DMC1-SSDS enrichment due to delayed DSB repair^{18,70,71}. Overall, this
319 indicates that the recruitment of DMC1 on ssDNA at SPO11-dependent DSB hotspots was efficient,
320 with relative hotspot intensities comparable to wild-type meiosis.

321

322 We then asked whether FIRRM depletion alters DMC1 extension on resected DSB ends at DSB
323 hotspots. To characterize precisely the DMC1-SSDS signal distribution across DSB hotspots, we defined
324 the center of overlapping SPO11-oligo hotspots as the center of our DMC1-SSDS peaks⁷⁰. This
325 improved significantly the quality of the average DMC1-SSDS signal profile, revealing a non-identical
326 distribution in control and *Firrm* cKO (Extended Data Fig. 7b-c). Especially, we clearly observed a
327 shoulder in the region of the curve surrounding the summit in control samples, as reported before,
328 suggestive of a control mechanism ensuring a minimal DMC1 nucleoprotein filament length^{18,70}. This
329 shoulder was strongly reduced in *Firrm* cKO testes (Fig. 6e, Extended Data Fig. 7c). To improve the
330 profile comparison, we normalized the overall signal intensity within common peaks in control and
331 *Firrm* cKO samples and plotted the strand-specific average profiles of the normalized DMC1-SSDS
332 signals (Fig. 6f). This confirmed that in *Firrm* cKO samples, DMC1-SSDS intensity started to progressively
333 decrease immediately next to the narrow peaks that marked the 3' end of the ssDNA tails. This profile
334 alteration was not dependent on the hotspot strength (Extended Data Fig. 7e). We also detected the
335 same alteration at X chromosome hotspots, suggesting that this was not just a consequence of delayed
336 DSB repair (Extended Data Fig. 7d). Moreover, the tail of DMC1 distribution extended a little further
337 away. This wider distribution might be explained by more frequent longer DMC1 filaments, or by
338 increased deposition of short DMC1 patches spread throughout the ssDNA tail. Altogether, the altered
339 profile in *Firrm* cKO spermatocytes suggests that DMC1 recruitment at DSB sites remains efficient on
340 a short DSB-proximal interval close to the 3' end of ssDNA tails independently of FIRRM, but that the
341 mechanism controlling the DMC1 filament length requires FIRRM for full efficiency. One possible

342 scenario is that the FIGNL1-FIRRM complex controls the balance between DMC1 and RAD51 loading
343 on ssDNA. Alternatively, we cannot exclude that the extent of DSB resection is altered.

344

345 ***Firrm* cKO is epistatic to *Swsap1* for controlling RAD51 and DMC1 loading**

346 In mouse meiosis, the Shu complex component SWSAP1 is required for the assembly of normal
347 numbers RAD51 and DMC1 foci, which are 2- to 3-fold fewer in *Swsap1*^{-/-} than in wild-type leptotene-
348 zygotene spermatocytes^{40,41}. FIGNL1 depletion suppresses the defect of human SWSAP1-depleted
349 cells in forming DNA damage-induced RAD51 foci, suggesting that SWSAP1 antagonizes the anti-RAD51
350 activity of FIGNL1⁴¹. We generated *Swsap1*^{-/-} *Firrm* cKO and *Swsap1*^{-/-} *Figl1* cKO double mutant mice
351 to determine if the defect in forming meiotic RAD51 and DMC1 foci in *Swsap1*^{-/-} spermatocytes is
352 similarly dependent on FIGNL1-FIRRM. We found that synapsis was defective and meiosis did not
353 progress further than the zygotene-like stage with partial, partly non-homologous synapses in *Swsap1*^{-/-}
354 *Firrm* cKO and *Swsap1*^{-/-} *Figl1* cKO spermatocytes, like in *Firrm* cKO and *Figl1* cKO single mutants.
355 A small subset of nuclei progressed to pachynema, as observed for *Swsap1*^{-/-} spermatocytes, most likely
356 due to incomplete *Firrm* or *Figl1* deletion. The double mutant spermatocytes accumulated RAD51
357 and DMC1, like *Firrm* cKO and *Figl1* cKO spermatocytes (Fig. 7a-d, Extended Data Fig. 8a-c). However,
358 because RAD51 and DMC1 accumulation in *Firrm* cKO and *Figl1* cKO spermatocytes was essentially
359 DSB-independent, this finding did not allow determining whether *Firrm* or *Figl1* cKO relieves RAD51
360 and DMC1 recruitment at DSBs from SWSAP1 dependency. As a proxy for their localization at DSB sites,
361 we measured RAD51 and DMC1 colocalization with RPA2 in *Swsap1*^{-/-} *Figl1* cKO spermatocytes. The
362 fraction (Fig. 7e-f) of on-axis RPA2 foci colocalized with RAD51 and DMC1 was similar in control, in
363 *Figl1* cKO, and in *Swsap1*^{-/-} *Figl1* cKO spermatocytes (measured in one mouse per genotype).
364 Reciprocally, equivalent numbers and fractions of on-axis RAD51 or DMC1 foci colocalized with RPA2
365 in *Figl1* cKO and in *Swsap1*^{-/-} *Figl1* cKO spermatocytes (Extended Data Fig. 8d-e and 8f-g,
366 respectively). Although the *Swsap1*^{-/-} single mutant was missing in this experiment, the number of on-
367 axis RAD51 or DMC1 foci colocalized with RPA2 exceeded the total number of RAD51 or DMC1 foci
368 reported in leptotene-zygotene *Swsap1*^{-/-} spermatocytes^{40,41}. This suggests that the formation of
369 detectable RAD51 and DMC1 foci at meiotic DSB sites might be independent of SWSAP1 in *Figl1* cKO
370 spermatocytes.

371

372 **FIGNL1 perturbs the structure of RAD51/DMC1 nucleoprotein filaments and inhibits RAD51- and** 373 **DMC1-mediated D-loop formation *in vitro***

374 To determine the HR step(s) in which FIGNL1-FIRRM might be involved, we examined *in vitro* the effect
375 of adding FIGNL1 on the assembly and stability of RAD51 and DMC1 nucleofilaments, and on their
376 subsequent strand invasion activity. We incubated preformed RAD51 or DMC1 filaments assembled

377 on a 400 nucleotide (nt) ssDNA or a 400 bp dsDNA with purified human FIGNL1 Δ N (Extended Data Fig.
378 9a). FIGNL1 Δ N did not promote RAD51 and DMC1 displacement from DNA (electrophoretic mobility
379 shift assay in Fig. 8a-b, pre-formed nucleofilament), but induced the formation of a higher molecular
380 weight complex, suggesting that FIGNL1 Δ N binds to RAD51/DMC1-DNA filaments. When we mixed
381 FIGNL1 Δ N with RAD51 or DMC1 before addition to the DNA substrate, we observed a slight increase
382 in the fraction of free dsDNA (but not ssDNA) that was not complexed with RAD51 or DMC1 (Figure
383 8a-c, no pre-formed nucleofilament). Whereas this increase was not significant, it might suggest that
384 the presence of FIGNL1 Δ N restricts RAD51 and DMC1 binding to DNA and the subsequent filament
385 elongation. We then used transmission electron microscopy (TEM) to analyze the effect on RAD51
386 filament formation and architecture upon addition of FIGNL1 Δ N at same time as RAD51 to a 400 nt
387 ssDNA (Fig. 8d-e). Addition of FIGNL1 Δ N induced the formation of super-complexes that contained
388 several bridged or interwoven filaments. Simultaneously, we observed that individual RAD51 filaments
389 not included in the super-complexes were significantly shorter than RAD51 filaments in controls (mean
390 length of 135 versus 175 nm, respectively; Fig. 8f, Extended Data Fig. 9b). We also detected the
391 formation of some very long filaments (more than 450 nm and up to 3-4 μ m). Their length was not
392 compatible with the length of the used DNA substrate, suggesting a DNA-independent polymerization
393 in the presence of FIGNL1 Δ N, which was confirmed by incubating RAD51 with FIGNL1 Δ N without DNA
394 (Extended Data Fig. 9b-d). Similarly, the mean length of RAD51 filaments assembled on a 400 bp dsDNA
395 decreased from 194 nm in control to 137 nm in the presence of FIGNL1 Δ N (Fig. 8f). The architecture
396 of DMC1 filament assembled both on ssDNA and on dsDNA displayed qualitatively similar alteration
397 (Extended Data Fig. 9c-d). Altogether, these results show that FIGNL1 Δ N limits RAD51/DMC1 assembly
398 on ssDNA and also dsDNA, and affect the filament architecture. We then tested whether these
399 filaments could pair with homologous donor dsDNA (pUC19 plasmid) in a D-loop assay. Preformed
400 RAD51, DMC1, and mixed RAD51-DMC1 filaments mediated the formation of 34, 27 and 22% of D-loop
401 products, respectively. Addition of FIGNL1 Δ N during filament assembly led to a decrease in the D-loop
402 yield (Fig. 8g-h). When we titrated FIGNL1 Δ N in the D-loop reaction, the yield decreased linearly and
403 significantly (Fig. 8h). This showed that the contacting and pairing with homologous DNA of filaments
404 assembled in the presence of FIGNL1 Δ N might be affected. This indicates that by limiting the assembly
405 of RAD51 and/or DMC1 on DNA, FIGNL1 could negatively regulate the next strand invasion step
406 required for HR.

407

408 **Discussion**

409

410 The AAA-ATPase FIGL1 and its partner FIRRM were identified recently as negative regulators of meiotic
411 COs in plants ^{44,47-49}, and FIGNL1 as a negative regulator of RAD51 in human cells ^{41,43}, but their role in
412 mammalian meiosis remained unknown. Here, by characterizing male germ line-specific *Figl1* and
413 *Firrm* cKO mouse models, we uncovered two roles of the FIGNL1-FIRRM complex in male meiosis. First,
414 FIGNL1 and FIRRM are required for meiotic DSB repair and for homologous chromosome synapsis
415 during meiotic prophase I, and thus are essential for male mouse meiosis. Second, the FIGNL1-FIRRM
416 complex prevents DNA damage-independent accumulation of RAD51 and DMC1 on chromatin and
417 chromosome axes in spermatocyte nuclei during premeiotic replication and meiotic prophase I.
418 Shinohara's group reached similar conclusions by characterizing the *Figl1* cKO mouse in a study
419 reported in the accompanying article.

420

421 Our data show that FIGNL1 and FIRRM act as negative regulators of RAD51 and DMC1 during meiotic
422 recombination, a function evolutionarily conserved from plants to mammals. However, the role of
423 FIGNL1-FIRRM is much more crucial in mouse spermatogenesis than in *A. thaliana* and rice meiosis
424 where homologous chromosome synapsis and formation of ZMM-dependent type I COs are almost
425 normal in FIGNL1 and FIRRM mutants ^{44,47-50}. Plants and mammals show differences in their
426 requirement of specific HR pathways for meiotic DSB repair, homologous chromosome synapsis and
427 progression through meiotic cell cycle. These processes require DMC1, MSH4 and MSH5 in the mouse
428 ^{12-14,60,72}. Conversely, in *A. thaliana* and rice, meiotic DSBs are repaired by RAD51-dependent intersister
429 HR in *dmc1* mutants, homologous chromosome synapsis does not depend on MSH4-MSH5, and *dmc1*,
430 *msh4* and *msh5* mutant cells progress through meiotic prophase (reviewed in ⁷³). These differences
431 might explain why FIGNL1 or FIRRM deficiency might lead to a stronger phenotype in mice than in
432 plants. However, mouse *Figl1* cKO and *Firrm* cKO spermatocytes also displayed defects not seen in
433 plants, especially a massive, DNA damage-independent RAD51 and DMC1 accumulation and defects in
434 MSH4 focus formation. This suggests that the FIGNL1-FIRRM complex has additional functions in the
435 mouse within the shared framework of RAD51 and DMC1 negative regulation.

436

437 We found that in *Figl1* cKO and *Firrm* cKO spermatocytes, MSH4 focus formation and meiotic DSB
438 repair were impaired, RAD51 and DMC1 foci accumulated at unrepaired DSB sites, and homologous
439 synapsis was defective. These defects have been described in mutants in which strand invasion is
440 impaired (e.g. *Dmc1*^{-/-} mice that accumulate only RAD51, *Hop2*^{-/-}, *Mnd1*^{-/-} mice)^{5,6,60,72,74-76} and in
441 mutants in which strand invasion might be preserved but the HR intermediates are not efficiently
442 stabilized (e.g. *Hrob*^{-/-}, *Mcm8*^{-/-}, *Mcmd2*^{-/-}, *Msh4*^{-/-}, *Msh5*^{-/-} mice)^{12-14,77-80}. By altering the stability or
443 architecture of the nucleoprotein filament formed by RAD51/DMC1 on ssDNA and/or dsDNA, the
444 FIGNL1-FIRRM complex might play a role before or after strand invasion. In the case of a post-strand

445 invasion role, this complex might favor RAD51/DMC1 dissociation from dsDNA in the D-loop, a step
446 required for initiating DNA synthesis to extend the invading strand. In *S. cerevisiae*, the motor protein
447 Rad54 and its paralog Rdh54 are involved in removing RAD51/DMC1 from dsDNA following D-loop
448 formation^{28,32}. In the mouse, the meiotic function of RAD54 and its paralog RAD54B is not crucial
449 because *Rad54 Rad54b* double mutant mice are fertile, although they display persistent RAD51 foci
450 during meiotic prophase^{33,34}. Thus, additional factors can disassemble RAD51 and DMC1 from the D-
451 loop. The FIGNL1-FIRRM complex might promote RAD51/DMC1 dissociation from dsDNA after strand
452 invasion by destabilizing the filament. In our *in vitro* assay, human FIGNL1 Δ N could not dissociate
453 preformed RAD51/DMC1 filaments; however, the full length FIGNL1-FIRRM complex might possess a
454 stronger activity sufficient to dissociate RAD51/DMC1 efficiently. Alternatively, FIGNL1-FIRRM
455 complex -dependent RAD51/DMC1 filament alteration might render it sensitive to dismantling by
456 other factors. In addition to normal HR intermediate processing, the FIGNL1-FIRRM complex might also
457 dissociate unproductive or potentially toxic post-synaptic RAD51/DMC1 filaments, such as multiple
458 strand invasion or invasion on non-allelic repeated sequences^{81,82}.

459
460 In *Firrm* cKO spermatocytes, the average DMC1-SSDS signal profile at meiotic DSB hotspots was altered
461 in a way that suggests that FIRRM may be involved in regulating the length of DMC1-ssDNA filaments.
462 In wild-type mouse spermatocytes, the profile of DMC1-SSDS coverage at DSB hotspots and super-
463 resolution microscopy observations indicate that DMC1 typically occupies the DSB-proximal two-third
464 of the DSB 3' ssDNA end, and RAD51 the DSB-distal third of the same DSB 3' ssDNA end^{5,6,16,18,66,70}.
465 DMC1 and RAD51 segregation along ssDNA tails might result from the formation of a stable DMC1
466 filament or/and from the prevention of RAD51 loading on the 3' region of the ssDNA tail. In the context
467 of inhibited RAD51 catalytic activity during meiosis, interhomolog recombination relies on DMC1
468 catalytic activity¹⁸⁻²⁰. Therefore, defects in regulating the length or the continuity of the active DMC1
469 filament may affect the efficiency of interhomolog search⁸², the formation of a D-loop that can be
470 stabilized by MSH4-MSH5, and homologous chromosome synapsis. Several non-exclusive hypotheses
471 can be proposed to explain how the FIGNL1-FIRRM complex regulates the DMC1 filament on DSB 3'
472 ssDNA tails. First, RAD51 nuclear fraction was increased in *Figl1* cKO and *Firrm* cKO testes (Fig. 1a),
473 suggesting that RAD51 might outcompete DMC1 on ssDNA tails in these mutants. It has been
474 suggested that BRCA2 promotes RAD51 nuclear import by limiting the formation of cytoplasmic RAD51
475 polymers which cannot be mobilized⁸³. We also found that RAD51 forms DNA-independent filaments
476 in the presence of purified human FIGNL1 Δ N (Extended Data Fig. 9c-d). Therefore, the balance
477 between FIGNL1-FIRRM and BRCA2 might control the level of cytoplasmic RAD51 polymerization,
478 contributing to fine-tune RAD51 nuclear level (Fig. 8i, (i)). We could also suggest that the FIGNL1-FIRRM
479 complex has a more direct role in controlling the formation of RAD51 and DMC1 filaments at DSB

480 ssDNA overhangs, based on a previously proposed model (Fig. 8i, (iii))⁹. *In vitro*, RAD51 nucleates
481 randomly on ssDNA tracts, whereas DMC1 prefers to seed at a ds/ssDNA junctions or on a RAD51 patch
482 (by analogy with *S. cerevisiae*), and polymerizes specifically in the 5' to 3' direction⁸⁴. We hypothesize
483 that the FIGNL1-FIRRM complex may disassemble nascent RAD51-ssDNA patches that would otherwise
484 hamper DMC1 filament extension toward the 3' end of ssDNA tails. According to this hypothesis, the
485 formation of dispersed RAD51 patches in *Firrm* cKO spermatocytes would impede the polymerization
486 of extended DMC1 filaments and consequently reduce DMC1 occupancy in the 3' region of ssDNA tails.
487 Specific accessory factors (e.g. the SWSAP1-SWS1-SPIDR complex) might protect RAD51 from the
488 FIGNL1-FIRRM complex on the DSB-distal part of ssDNA tails. Indeed, the SWSAP1-SWS1-SPIDR
489 complex is required to form normal numbers of RAD51/DMC1 foci during meiosis^{36,40-42}. Moreover,
490 FIGNL1 interacts with SWSAP1 and SPIDR^{37,41,43}, and SWSAP1 protects RAD51 filaments from FIGNL1
491 *in vivo* and *in vitro*⁴¹. Interestingly, it was recently reported that in human cells, SWSAP1-SWS1 interact
492 with the cohesin regulatory protein PDS5B, which localizes to chromosome axes during meiotic
493 prophase^{37,85}. As generally RAD51 localizes closer to the chromosome axis than DMC1 in mouse
494 meiotic prophase^{18,66}, this interaction, if present in meiotic prophase, might provide an anchor that
495 favors preferential RAD51 protection on the DSB-distal part of DSB ssDNA tails. Alternatively, we
496 cannot exclude that DMC1-SSDS profile alterations are due to accumulating HR intermediates with a
497 biased DMC1-ssDNA distribution. For example, longer DMC1 filaments might be more frequently
498 engaged in strand invasion, therefore bound on dsDNA and undetectable by ChIP-SSDS, compared with
499 shorter filaments.

500

501 In *Figl1* cKO and *Firrm* cKO spermatocytes, we observed meiotic DSB-independent accumulation of
502 RAD51 foci on chromatin during premeiotic replication that persisted and was accompanied by DMC1
503 accumulation during meiotic prophase. DNA damage-independent RAD51 foci accumulate in human
504 cells upon RAD51 overexpression²⁹, thus higher RAD51 nuclear concentration in the absence of FIRRM
505 or FIGNL1 might contribute to favor DNA damage-independent RAD51 and DMC1 binding on intact
506 chromatin (Fig. 8i, (i)). In addition, RAD51 and DMC1 DNA damage-independent accumulation is
507 observed in budding yeast and human cells after depletion of RAD54 family DNA translocases²⁹⁻³¹. By
508 analogy, the FIGNL1-FIRRM complex might prevent the stabilization of normally transient nascent
509 RAD51-dsDNA filaments at replication forks (Fig. 8i, (ii)). This hypothesis is consistent with our finding
510 that purified human FIGNL1ΔN might reduce RAD51 and DMC1 association with dsDNA *in vitro* (Fig.
511 8b-c), and with a recent study in human cells showing FIGNL1-FIRRM association with ongoing
512 replication forks in unchallenging conditions⁸⁶.

513

514 The linear RAD51/DMC1 staining detected between SYCP3 synapsed axes suggests that RAD51/DMC1
515 can associate stably with chromosome axis components, in either a DNA-dependent or DNA-
516 independent manner, in the absence of the FIGNL1-FIRRM complex. DSB-independent RAD51 (but not
517 DMC1) staining along unsynapsed chromosome axes has been previously described in late prophase
518 mouse oocytes^{67,87,88}; however, these structures associating RAD51 and DMC1 along synapsed axes in
519 *Figl1* cKO and *Firrm* cKO spermatocytes are unusual. RAD51 interacts with several components of
520 meiotic chromosomes, including the axis component SYCP3¹⁵, the SC central element component
521 SYCE2^{89,90} and the cohesion regulator PDS5A/B^{91,92} that interacts also with SWSAP1-SWS1³⁷.
522 Interestingly, it has been observed by super-resolution microscopy that several cohesin subunits and
523 HORMAD1/2 coat the outside of SYCP3 axis cores^{66,93}, a localization resembling that of RAD51/DMC1
524 staining between synapsed SYCP3-positive axes. RAD51/DMC1 interactions with components of
525 meiotic chromosome axes might facilitate the accurate HR repair of meiotic DSBs (and incidental DNA
526 damages). In this context, a function of the FIGNL1-FIRRM complex might be to prevent the
527 stabilization, of these interactions, other than at DNA damage sites.

528

529 Meiotic cells must face the challenge of repairing hundreds of programmed DSBs through several HR
530 pathways, while restricting inappropriate repair that may involve similar HR intermediates. In this
531 study, we started deciphering the functions of the conserved FIGNL1-FIRRM complex in mouse
532 meiosis. We showed that the RAD51/DMC1 filament destabilizing activity of FIGNL1 and FIRRM is
533 implicated in regulating meiotic recombination and restricting inappropriate formation of stable
534 RAD51/DMC1 filaments. Interestingly, although FIGNL1 alters RAD51 and DMC1 filament similarly *in*
535 *vitro*, it is not clear whether FIGNL1 or FIRRM absence affects DMC1 directly or indirectly through
536 RAD51. The elucidation of the several possible functions of the FIGNL1- FIRRM complex during mouse
537 meiosis will need more *in vitro* and *in vivo* analyses of their functional interactions with other RAD51
538 and DMC1 regulators.

539

540

541 **Methods**

542 **Mice**

543 All mice used in the study were in the C57BL/6J background. *Firrm*^{fl/+} mice (allele
544 *BC055324*^{tm1c(EUCOMM)Hmgu}, MGI:5692863) were obtained from the International Knockout Mouse
545 Consortium (IKMC). *Figl1*^{fl/+} mice (allele *Figl1*^{tm1c(EUCOMM)Hmgu}) were generated by Phenomin-Institut
546 Clinique de la Souris (ICS) using the plasmid containing the *Figl1*^{tm1a(EUCOMM)Hmgu} allele (MGI:5287847)
547 obtained from Helmholtz Zentrum München GmbH. *Firrm*^{fl/fl} mice were mated with mice that express
548 Cre under the control of the CMV promoter (C57BL/6 Tg(CMV-cre)1Cgn)⁹⁴ to generate *Firrm*-deleted

549 heterozygous mice (*Firm^{+/-}*). *Firm^{+/-}* mice were mated with Tg(*Stra8-icre*)1Reb/J (*Stra8-Cre^{Tg}*) mice⁵²
550 to generate *Firm^{+/-};Stra8-Cre^{Tg}* mice. By crossing *Firm^{fl/fl}* mice with *Firm^{+/-};Stra8-Cre^{Tg}* mice, *Firm^{fl/-}*
551 *;Stra8-Cre^{Tg}* (*Firm* cKO) and *Firm^{fl/+}*, *Firm^{fl/+} Stra8-Cre^{Tg}* or *Firm^{fl/-}* (*Firm* control) mice were
552 obtained. *Figl1^{fl/-};Stra8-Cre^{Tg}* (*Figl1* cKO) mice were generated using the same strategy as for *Firm*
553 cKO mice. The *Spo11^{YF/YF}*⁶⁷ and *Swsap1^{-/-}*⁹⁵ mouse lines were described previously. Primers used for
554 genotyping are listed in Supplementary Table 1. All animal experiments were carried out according to
555 the CNRS guidelines.

556

557 **Histology**

558 Mouse testes were fixed in Bouin's solution for periodic acid-Schiff (PAS) staining at room temperature,
559 overnight. Testes were then embedded in paraffin and 3µm-thick slices were cut. PAS-stained sections
560 were scanned using the automated tissue slide-scanning tool of a Hamamatsu NanoZoomer Digital
561 Pathology system.

562

563 **Spermatocyte chromosome spreads**

564 Spermatocyte spreads were prepared with the dry down technique⁹⁶. Briefly, a suspension of testis
565 cells was prepared in PBS, and then incubated in a hypotonic solution for 8 min at room temperature.
566 Cells were centrifuged, resuspended in 66 mM sucrose solution and spread on slides or coverslips
567 (1.5H, high precision) with 1% paraformaldehyde, 0.05% Triton X-100. Slides/coverslips were dried in
568 a humid chamber for 1-2 h, washed in 0.24% Photoflo200 (Kodak), air-dried, and used for
569 immunostaining or stored at -80°C.

570

571 **Immunofluorescence staining**

572 Immunostaining was done as described⁹⁷. After incubation with a milk-based blocking buffer (5% milk,
573 5% donkey serum in PBS), spermatocyte spreads were incubated with primary antibodies at room
574 temperature overnight, followed by secondary antibodies (37 °C for 1 h). The used antibodies are listed
575 in Supplementary Table 2. Nuclei were stained with 4'-6-diamidino-2-phenylindole (DAPI, 2 µg/ml) in
576 the final washing step.

577 For immunostaining with the anti-DMC1 antibody, a specific blocking buffer (0.5% BSA, 0.5% powder
578 milk, 0.5% donkey serum in PBS) was used prior to incubation with the primary antibody that was
579 performed in 10% BSA in PBS. Immunostaining of spermatocyte spreads on coverslips for STED
580 microscopy was done with specific secondary antibodies (Supplementary Table 2), and DAPI was
581 omitted.

582

583 **Widefield fluorescent imaging**

584 Widefield images were acquired using one of the following microscopes: Zeiss Axioimager Apotome
585 with 100X Plan Achromat 1.46 oil DIC objective and 1 ANDOR sCMOS ZYLA 4.2 MP monochrome
586 camera (2048 x 2048 pixels, 6.5 μ m pixel size) or Zeiss Axioimager 100X Plan Achromat 1.4 NA oil
587 objective and 1 Zeiss CCD AxioCam Mrm 1.4 MP monochrome camera (1388 x 1040 pixels, 6.45 μ m
588 pixel size).

589

590 **Stimulated emission depletion (STED) super-resolution imaging**

591 Super-resolution images were acquired using a STED microscope (Abberior Instruments, Germany)
592 equipped with a PlanSuperApo 100x/1.40 oil immersion objective (Olympus, Japan). For 3-color STED
593 imaging, immunolabeling was performed using one of the following combinations of secondary
594 antibodies: STAR 460L, STAR ORANGE, STAR RED or STAR GREEN, STAR ORANGE, STAR RED
595 (Supplementary Table 2). STAR 460L and STAR 488 were excited at 485nm, STAR ORANGE at 561nm,
596 and STAR RED at 640nm. Excitation was done with a dwell time of 10 μ s. STED was performed at 595
597 nm for STAR 488 and at 775nm for all other dyes. Images were collected in line accumulation mode
598 with detection set at 571-625nm for STAR 460L and STAR ORANGE, 500-580nm for STAR GREEN, and
599 650-750nm for STAR RED.

600

601 **Image analysis**

602 For quantification and colocalization analyses, images were deconvolved using Huygens Professional
603 version 22.10 (Scientific Volume Imaging).

604 All image analyses were performed using Fiji/ImageJ 1.53t⁹⁸.

605 Single nuclei were cropped manually or using an automatic DAPI signal threshold. Nuclei were sorted
606 into meiotic prophase substages following the criteria described below.

607 Foci were detected using the Find Maxima function. On-axis and off-axis foci were distinguished on the
608 basis of their localization within (or outside) a binary mask. This ROI was drawn using an automatic
609 SYCP3 axis protein staining threshold (SYCP1 staining was used for MSH4 and TEX11 foci). Because
610 there was no SYCP3 staining-defined axis structure at preleptotene stage, all foci were considered as
611 off-axis foci at this stage.

612 For two-color focus colocalization, the distance of a given channel focus to the closest second color
613 focus was calculated. Foci were considered as colocalized when this distance was below the minimum
614 resolution distance (0.3 μ m for widefield images), as in⁹⁹. The level of random colocalization of foci in
615 channel A (foci A) with foci in channel B (foci B) in any given nucleus was estimated by simulating the
616 random localization of the actual number of foci A, and by determining the number of random foci A
617 colocalized with actual foci B. The mean number of colocalizations from 100 simulations was taken as

618 the number of foci A colocalized with foci B by chance in the nucleus (n_{random} , “random” on figures),
619 and this was repeated for every nucleus. Reciprocally, the level of random colocalization of foci B with
620 foci A resulted from random simulations of foci B localizations.

621 In every nucleus, the number of colocalized foci A was corrected for random colocalization by
622 considering that (1) the observed number of colocalized foci A (n_{obs}) is composed of one subset of
623 biologically meaningful colocalized foci (“truly” colocalized foci A, n_{col}) and one subset of foci A
624 colocalized by chance; (2) the ratio $n_{\text{random}}/n_{\text{T}}$ (where n_{random} is estimated as described above and n_{T} is
625 the total number of foci A in the nucleus) estimates the frequency of foci A colocalizing by chance
626 among the population of foci A not “truly” colocalized, thus the number of foci A colocalized by chance
627 is $(n_{\text{T}} - n_{\text{col}}) * n_{\text{random}}/n_{\text{T}}$, by excluding the truly colocalized foci A from random colocalization.(3) Finally,
628 the estimated number of colocalized foci corrected for random colocalization (n_{col}) was obtained from
629 the formula $n_{\text{col}}=(n_{\text{obs}}-n_{\text{random}})/(n_{\text{T}}-n_{\text{random}})$, where n_{tot} was the total number of foci counted, n_{obs} the
630 observed number of colocalized foci and n_{random} the mean number of colocalization from 100
631 simulations as described above. The percentage of corrected colocalization estimate was the ratio of
632 the corrected number of colocalized foci n_{col} over the total number of foci in the same nucleus, $n_{\text{col}} /$
633 n_{T} .

634 For γ H2AX quantification, nuclei were cropped manually and the integrated intensity of the γ H2AX
635 channel in the cropped region was measured.

636 Prophase spermatocytes were staged using the following criteria, based on SYCP3 staining.
637 Preleptotene nuclei had patchy weak SYCP3 signal throughout the nucleus. Early leptotene nuclei had
638 focus-like well-defined very short stretches of SYCP3 staining. Leptotene nuclei had short stretches of
639 SYCP3 fragments. Early zygotene nuclei had longer SYCP3 stretches as the chromosome axes continued
640 to elongate. Mid-zygotene nuclei had very long or full SYCP3 axes, but no or relatively few synapses
641 marked by thicker SYCP3 stretches. Late zygotene had full SYCP3 axes with extensive synapsis marked
642 by thicker SCP3 signal.

643

644 **DMC1 chromatin immuno-precipitation, followed by single-strand DNA sequencing (DMC1-SSDS)**

645 DMC1 ChIP-SSDS and library preparation were performed as described in ¹⁰⁰ using a goat anti-DMC1
646 antibody (0.5 mg/ml; Santa Cruz, reference C-20). Ten testes from 12 dpp *Firm^{fl/+};Stra8-Cre^{Tg}* (control)
647 and from *Firm^{fl/+};Stra8-Cre^{Tg}* (*Firm* cKO) mice were used in each biological replicate. Sequencing was
648 performed on a NovaSeq 6000 PE150 platform in paired end mode (2x150bp).

649

650 **Detection of DMC1 ChIP-SSDS peaks**

651 Raw reads were processed using the SSDS-DMC1 Nextflow pipeline (Auffret et al., MiMB Germ Cells
652 Development, in prep.), available on github (<https://github.com/jajclement/ssdsnextflowpipeline>, see
653 details of the pipeline development on the README page). Briefly, the main steps of the pipeline
654 included raw read quality control and trimming (removal of adapter sequences, low-quality reads and
655 extra bases) and mapping to the UCSC mouse genome assembly build GRCm38/mm10. Single stranded
656 derived fragments were then identified from mapped reads using a previously published method^{68,101},
657 and peaks were detected in Type-1 fragments (high confidence ssDNA). To control reproducibility and
658 assess replicate consistency, the Irreproducible Discovery Rate (IDR) method¹⁰² was used, following
659 the ENCODE procedure (<https://github.com/ENCODE-DCC/chip-seq-pipeline2>). The “regionPeak” peak
660 type parameter and default p-value thresholds were used. Briefly, this method performs relaxed peak
661 calling for each of the two replicates (truerep), the pooled dataset (poolrep), and pseudo-replicates
662 that are artificially generated by randomly sampling half of the reads twice, for each replicate and the
663 pooled dataset. Both control and *Firrm* cKO datasets passed the IDR statistics criteria for the two scores
664 (well below 2). By default, the pipeline gave the poolrep as primary output, but for this study the
665 truerep peak sets were considered. Lastly, peak centering and strength calculation were computed
666 using a previously published method⁶⁸.

667 The list of SPO11-oligo hotspots from B6 mice and the coordinates (genome build GRCm38/mm10) of
668 their center were from⁷⁰.

669 The overlaps between intervals was determined with bedtools¹⁰³ Intersect on the Galaxy France web
670 interface. For determining overlaps between control and *Firrm* cKO peaks, a minimum overlap of 10%,
671 and reciprocally, was required. The overlap between DMC1-SSDS peaks and the center of SPO11-oligo
672 hotspots⁷⁰ was considered positive if at least 1 bp of the DMC1-hotspot contained the coordinate of
673 the center of one SPO11-oligo hotspot.

674 Heatmaps and average plot profiles were generated with deeptools (computeMatrix, plotHeatmap
675 and PlotProfile) on Galaxy France server.

676

677 **Preparation of mouse testis protein extracts and western blotting**

678 Cytoplasmic and nuclear extracts were prepared from 12 dpp control, *Firrm* cKO and *Figl1* cKO mice.
679 Testes were homogenized in hypotonic buffer (10 mM Hepes, pH 7.4, 320 mM sucrose, 0.2 mM PMSF,
680 1x Complete protease inhibitor cocktail, EDTA-free (Roche), 0.07% beta-mercaptoethanol) in a Dounce
681 homogenizer. After centrifugation (1,000xg at 4°C for 10 min), the supernatant was collected and used
682 as cytoplasmic fraction. The pellet was resuspended in half nuclear packed volume of low salt buffer
683 (20mM Tris-HCl pH7.3, 12.5% glycerol, 1.5mM MgCl₂, 0.2mM EDTA, 20mM KCl, 1x Complete protease
684 inhibitor cocktail, EDTA-free (Roche), 0.07% beta-mercaptoethanol). Then half nuclear packed volume
685 of high salt buffer (same, but 1.2M KCl) was added drop by drop, incubated at 4°C for 30min with

686 agitation and centrifuged (14,000xg at 4°C for 30 min). The supernatant was collected as nuclear
687 fraction. Cytoplasmic and nuclear fractions were analyzed by western blotting with rabbit anti-FIGNL1
688 (1/500, Proteintech, 17604-1-AP), rabbit anti-FIRRM (1/500, Abcam, ab121774), rabbit anti-beta
689 tubulin (1/3000, Abcam, ab6046) and guinea pig anti-SYCP3 (1/3,000⁹⁷) antibodies. HRP-conjugated
690 secondary antibodies were anti-rabbit IgG-HRP (1:5,000; Cell Signaling Technology) and donkey anti-
691 guinea pig IgG-HRP (1/10,000; Jackson Immuno Research, 706-035-148).

692

693 **Protein purification.** Human RAD51 was purified by the CiGEX Platform (CEA, Fontenay-aux-Roses) as
694 follows. His-SUMO-RAD51 was expressed in the *E. coli* strain BRL (DE3) pLys. All protein purification
695 steps were carried out at 4°C. Cells from a 3-liter culture that was induced with 0.5 mM isopropyl-1-
696 thio-β-D-galactopyranoside (IPTG) at 20°C overnight were resuspended in 1x PBS, 350 mM NaCl, 20
697 mM imidazole, 10% glycerol, 0.5 mg/ml lysozyme, Complete Protease Inhibitor (Roche), 1 mM 4-(2-
698 aminoethyl)benzenesulfonyl fluoride (AEBSF). Cells were lysed by sonication and the insoluble material
699 was removed by centrifugation at 150,000 x g for 1h. The supernatant was incubated with 5 ml of Ni-
700 NTA resin (Qiagen) for 2h. The mixture was poured into an Econo-Column Chromatography Column
701 (BIO-RAD) and beads were washed first with 80 ml W1 buffer (20 mM Tris HCl pH 8, 500 mM NaCl, 20
702 mM imidazole, 10% glycerol, 0.5% NP40), followed by 80 ml of W2 buffer (20mM Tris HCl pH 8, 100mM
703 NaCl, 20mM imidazole, 10% glycerol, 1 mM DTT). Then, His-SUMO-RAD51 bound to the beads was
704 resuspended in 8ml of W2 buffer and incubated with SUMO protease at a 1/80 ratio (w/w) for 16 h.
705 RAD51 without the His-SUMO tag was then recovered into the flow thru and directly loaded onto a
706 HiTrap heparin column (GE Healthcare). The column was washed with W2 buffer and then a 0.1-1M
707 NaCl gradient was applied. Fractions containing purified RAD51 were concentrated and dialyzed
708 against storage buffer (20mM Tris HCl pH 8, 50mM KCl, 0.5 mM EDTA, 10% glycerol, 1 mM DTT, 0.5
709 mM AEBSF) and stored at -80°C. Human RPA was purified by the CiGEX Platform (CEA, Fontenay-aux-
710 Roses) as previously described¹⁰⁴.

711 For human FIGNL1 purification, *FIGNL1ΔN* without the region encoding the N-terminal 284 aa was
712 inserted into the pET15 vector (Novagene), and the protein was overexpressed in *E. coli* BL21(DE3)
713 cells upon addition of 0.2mM IPTG at 37°C for 3h. Cell pellets were resuspended in buffer A (50mM
714 Tris-HCl pH7.4, 500 mM NaCl, 5% glycerol, 5mM MgCl₂, 5 mM β-mercaptoethanol, 1 mM PMSF, 0.1%
715 NP40, 20 mM imidazole, cOmplete Protease Inhibitor Cocktail), disrupted by French press (6 bar) and
716 cleared by centrifugation following incubation with the benzonase nuclease (Sigma) at 4°C for 30 min.
717 The supernatant was loaded on a 1 ml HisTrap Fast-Flow column (GE healthcare) and equilibrated with
718 buffer A on an ÄKTA pure system. After a washing step, proteins were eluted with buffer A
719 supplemented with 300 mM imidazole. FIGNL1ΔN was further purified by size exclusion
720 chromatography using a HiLoad 16/600 Superdex 200 column (GE Healthcare) in buffer B (50mM Tris-

721 HCl pH7.4, 200 mM NaCl, 10% glycerol, 5mM MgCl₂, 5 mM β-mercaptoethanol). The peak fractions
722 were concentrated with Amicon Ultra 30K (Millipore) and stored at -80°C.

723

724 **RAD51 and DMC1 filament electromobility shift assay (EMSA).** RAD51 and DMC1 filaments were
725 formed by incubating 3 μM (nucleotide concentration) of 400 nt ssDNA or dsDNA labeled with Cy5
726 with 1 μM RAD51 (1 protein per 3 nt) or 1.5 μM DMC1 (>1 protein per 3 nt to obtain fully covered
727 DNA) in a buffer containing 10 mM Tris-HCl pH7.5, 50 mM NaCl, 2 mM MgCl₂, 2 mM CaCl₂, 2 mM ATP,
728 and 1 mM DTT at 37°C for 20 min. Then, 1.6 μM of FIGLN1ΔN was added to the reaction to test their
729 effects on filament assembly and architecture (pre-formed filament). Alternatively, RAD51 or DMC1
730 was added concomitantly with FIGLN1ΔN to the reaction (no pre-formed filament). Protein-DNA
731 complexes were fixed in 0.01% glutaraldehyde at room temperature for 5 min. Then, the reaction
732 products were analyzed using 1% agarose gel in 0.5x Tris acetate/EDTA at 4 °C. Images were acquired
733 using a Typhoon imager (GE Healthcare Life Science).

734

735 **Transmission electron microscopy (TEM) analysis of RAD51 and DMC1 filaments.** RAD51 and DMC1
736 filaments were formed by incubating 7.5 μM (nucleotide concentration) of 400 nt long ssDNA and
737 dsDNA with 2.5 μM RAD51 (1 protein per 3 nt) or 3.5 μM DMC1 in a buffer containing 10 mM Tris-HCl
738 pH7.5, 50 mM NaCl, 2 mM MgCl₂, 2 mM CaCl₂, 2 mM ATP and 1 mM DTT at 37°C for 20 min. Then, 1.6
739 μM of FIGLN1ΔN was added to the reaction at the same time as RAD51/DMC1. For filament length
740 analysis, positive staining combined with a TEM dark-field imaging mode were used: 1 μL of the
741 reaction was quickly diluted 20 times in a buffer containing 10 mM Tris-HCl pH 7.5, 50 mM NaCl, 2 mM
742 MgCl₂, 2 mM CaCl₂. During one minute, a 5 μL drop of the dilution was deposited on a 600-mesh copper
743 grid previously covered with a thin carbon film and pre-activated by glow-discharge in the presence of
744 amylamine (Sigma-Aldrich, France) ^{105,106}. Grids were rinsed and positively stained with aqueous 2 %
745 (w/v) uranyl acetate, dried carefully with a filter paper. To better observe FIGLN1ΔN effect on the
746 filament architecture, samples were also spread using negative staining and observed in bright-field
747 mode. For this, a drop of the reaction was directly deposited on a carboned copper grid pre-activated
748 with glow discharge (plasma).

749 TEM grids were observed in the annular dark-field mode in zero-loss filtered imaging or in canonical
750 bright-field imaging using a Zeiss 902 transmission electron microscope. Images were captured at a
751 magnification of 85,000× with a Veleta CCD camera and analyzed with the iTEM software (both
752 Olympus Soft Imaging Solution). For quantification, the filament length was measured in at least two
753 independent experiments with a total of at least 75 molecules measured.

754

755 **D-loop *in vitro* assay.** RAD51 and DMC1 filaments were formed in the same conditions as for the EMSA
756 analysis. The same incubation conditions and buffer were used to assemble mixed RAD51/DMC1
757 filaments by incubating 3 μ M (nucleotide concentration) of 400 nt ssDNA substrates with 1.25 μ M
758 RAD51 plus 0.75 μ M DMC1. In the second step, 15 nM in molecules of homologous dsDNA donor
759 (pUC19 plasmid purified on MiniQ ion exchange chromatography column) was introduced in the
760 reaction and in case of DMC1 filaments, 4 mM more CaCl₂ was added, and then the mixture was
761 incubated at 37°C for 30 min. The reaction was stopped with 0.5 mg/mL proteinase K, 1% SDS, 12.5
762 mM EDTA at 37°C for 30 min and separated on 1% TAE agarose gels (80 V, for 30 min).

763

764 **Statistical analysis and reproducibility**

765 The statistical analyses of cytological observations were done with GraphPad Prism 9. A contingency
766 chi-square test was used to compare stage distributions. The nonparametric Mann-Whitney test was
767 used to compare focus counts, colocalized focus counts and fractions, and γ H2AX intensity among
768 genotypes. The nonparametric Wilcoxon signed-ranks test was used to compare true colocalization
769 versus random colocalization of foci. All tests, sample size, and p values (n.s., not significant, *P < 0.05,
770 **P < 0.01, ***P < 0.001, ****P < 0.0001) are provided in the corresponding legends and/or figures. If
771 not otherwise stated, at least two animals/genotype were analyzed and similar results were obtained.

772

773 **Data availability**

774 The DMC1-SSDS raw and processed data for this study have been deposited in the European
775 Nucleotide Archive (ENA) at EMBL-EBI and are available through the project identifier PRJEB62127.

776

777 **Acknowledgements**

778 We would like to thank Masaru Ito and Akira Shinohara for sharing unpublished results, Maria Jasin for
779 *Swsap1* mice, Qinghua Shi for the guinea-pig anti-DMC1 antibody. We thank Raphaël Mercier for
780 encouraging the project, and Thomas Robert for critical reading of the manuscript. We thank the
781 following Montpellier Biocampus facilities for their service: Anne Sutter and the animal facility (RAM)
782 for animal care, Manon Leportier for managing our mouse strains, the Réseau d'Histologie
783 Expérimentale de Montpellier (RHEM) for histology. We acknowledge the support of Marie-Pierre
784 Blanchard for help with STED microscopy and the imaging facility MRI, member of the national
785 infrastructure France-BioImaging infrastructure supported by the French National Research Agency
786 (ANR-10-INBS-04, "Investments for the future"). We are grateful to Xavier Veaute from the CiGEX
787 Platform (CEA, Fontenay-aux-Roses), and to the <https://www.france-bioinformatique.fr/> and the
788 <https://www.france-bioinformatique.fr/fr/cluster> for providing computing resources on Galaxy
789 France.

790 This work was supported by the Agence Nationale de la Recherche ANR FIRE (ANR-17-426 CE12-0015)
791 to FB, PD, JBC and RK; by the Ligue contre le Cancer (Comité départemental de l'Hérault and Comité
792 départemental du Gard) to FB; by the Ligue contre le Cancer (MB/CB/070-22) to RK. AZ was funded by
793 ANR FIRE (ANR-17-426 CE12-0015) and a PhD fellowship FDT202106012805 from the Fondation pour
794 la Recherche Médicale (FRM).

795

796 **Author contributions**

797

798 AZ, PD, RK and FB conceived and designed the experiments. AZ performed most mouse experiments,
799 SB and FB performed some mouse experiments. AZ and FB interpreted and analyzed mouse data with
800 input from BdM. PD, VR, RK performed, analyzed and interpreted biochemical experiments with
801 contribution from JBC. JC developed the method for image analysis. PA and JAJC developed the
802 bioinformatic pipeline for analyzing SSSDs data. JAJC and FB performed bioinformatic analysis of SSSD
803 data. AZ, PD, RK and FB wrote the manuscript with input from all authors.

804

805 **Competing interests**

806 The authors declare no competing interests.

807

808 **References**

- 809 1. Gerton, J. L. & Hawley, R. S. Homologous chromosome interactions in meiosis: diversity amidst
810 conservation. *Nat Rev Genet* **6**, 477–487 (2005).
- 811 2. Hunter, N. Meiotic Recombination: The Essence of Heredity. *Cold Spring Harb Perspect Biol* **7**,
812 a016618 (2015).
- 813 3. Baudat, F., Imai, Y. & de Massy, B. Meiotic recombination in mammals: localization and
814 regulation. *Nat Rev Genet* **14**, 794–806 (2013).
- 815 4. Robert, T., Vrielynck, N., Mézard, C., de Massy, B. & Grelon, M. A new light on the meiotic DSB
816 catalytic complex. *Seminars in Cell & Developmental Biology* **54**, 165–176 (2016).
- 817 5. Paiano, J. *et al.* ATM and PRDM9 regulate SPO11-bound recombination intermediates during
818 meiosis. *Nature Communications* **11**, (2020).
- 819 6. Yamada, S. *et al.* Molecular structures and mechanisms of DNA break processing in mouse
820 meiosis. *Genes & development* **34**, 806–818 (2020).

- 821 7. Prakash, R., Zhang, Y., Feng, W. & Jasin, M. Homologous Recombination and Human Health: The
822 Roles of BRCA1, BRCA2, and Associated Proteins. *Perspectives in Biology* 1–29 (2015)
823 doi:10.1101/cshperspect.a016600.
- 824 8. Zelensky, A., Kanaar, R. & Wyman, C. Mediators of Homologous DNA Pairing. *Cold Spring Harb*
825 *Perspect Biol* **6**, a016451 (2014).
- 826 9. Brown, M. S. & Bishop, D. K. DNA strand exchange and RecA homologs in meiosis. *Cold Spring*
827 *Harb Perspect Biol* **7**, a016659 (2014).
- 828 10. Börner, G. V., Kleckner, N. & Hunter, N. Crossover/Noncrossover Differentiation, Synaptonemal
829 Complex Formation, and Regulatory Surveillance at the Leptotene/Zygotene Transition of
830 Meiosis. *Cell* **117**, 29–45 (2004).
- 831 11. Pyatnitskaya, A., Borde, V. & De Muyt, A. Crossing and zipping: molecular duties of the ZMM
832 proteins in meiosis. *Chromosoma* **128**, 181–198 (2019).
- 833 12. Kneitz, B. *et al.* MutS homolog 4 localization to meiotic chromosomes is required for
834 chromosome pairing during meiosis in male and female mice. *Genes Dev* **14**, 1085–1097 (2000).
- 835 13. Edelman, W. *et al.* Mammalian MutS homologue 5 is required for chromosome pairing in
836 meiosis. *Nat Genet* **21**, 123–127 (1999).
- 837 14. de Vries, S. S. *et al.* Mouse MutS-like protein Msh5 is required for proper chromosome synapsis
838 in male and female meiosis. *Genes Dev* **13**, 523–531 (1999).
- 839 15. Tarsounas, M., Morita, T., Pearlman, R. E. & Moens, P. B. Rad51 and Dmc1 Form Mixed
840 Complexes Associated with Mouse Meiotic Chromosome Cores and Synaptonemal Complexes.
841 *Journal of Cell Biology* **147**, 207–220 (1999).
- 842 16. Slotman, J. A. *et al.* Super-resolution imaging of RAD51 and DMC1 in DNA repair foci reveals
843 dynamic distribution patterns in meiotic prophase. *PLOS Genetics* **16**, e1008595 (2020).
- 844 17. Brown, M. S., Grubb, J., Zhang, A., Rust, M. J. & Bishop, D. K. Small Rad51 and Dmc1 Complexes
845 Often Co-occupy Both Ends of a Meiotic DNA Double Strand Break. *PLOS Genetics* **11**, e1005653
846 (2015).

- 847 18. Hinch, A. G. *et al.* The Configuration of RPA, RAD51, and DMC1 Binding in Meiosis Reveals the
848 Nature of Critical Recombination Intermediates. *Molecular Cell* (2020)
849 doi:10.1016/j.molcel.2020.06.015.
- 850 19. Cloud, V., Chan, Y.-L., Grubb, J., Budke, B. & Bishop, D. K. Rad51 is an accessory factor for Dmc1-
851 mediated joint molecule formation during meiosis. *Science (New York, N.Y.)* **337**, 1222–5 (2012).
- 852 20. Da Ines, O. *et al.* Meiotic Recombination in Arabidopsis Is Catalysed by DMC1, with RAD51 Playing
853 a Supporting Role. *PLoS Genetics* **9**, (2013).
- 854 21. Halder, S. *et al.* Double-stranded DNA binding function of RAD51 in DNA protection and its
855 regulation by BRCA2. *Molecular Cell* **82**, 3553-3565.e5 (2022).
- 856 22. Mason, J. M., Chan, Y.-L., Weichselbaum, R. W. & Bishop, D. K. Non-enzymatic roles of human
857 RAD51 at stalled replication forks. *Nat Commun* **10**, 4410 (2019).
- 858 23. Schlacher, K. *et al.* Double-Strand Break Repair-Independent Role for BRCA2 in Blocking Stalled
859 Replication Fork Degradation by MRE11. *Cell* **145**, 529–542 (2011).
- 860 24. Berti, M., Cortez, D. & Lopes, M. The plasticity of DNA replication forks in response to clinically
861 relevant genotoxic stress. *Nat Rev Mol Cell Biol* **21**, 633–651 (2020).
- 862 25. Kolinjivadi, A. M. *et al.* Moonlighting at replication forks – a new life for homologous
863 recombination proteins BRCA1, BRCA2 and RAD51. *FEBS Letters* **591**, 1083–1100 (2017).
- 864 26. Hashimoto, Y., Ray Chaudhuri, A., Lopes, M. & Costanzo, V. Rad51 protects nascent DNA from
865 Mre11-dependent degradation and promotes continuous DNA synthesis. *Nat Struct Mol Biol* **17**,
866 1305–1311 (2010).
- 867 27. Reitz, D., Chan, Y.-L. & Bishop, D. K. How strand exchange protein function benefits from ATP
868 hydrolysis. *Curr Opin Genet Dev* **71**, 120–128 (2021).
- 869 28. Ceballos, S. J. & Heyer, W.-D. Functions of the Snf2/Swi2 family Rad54 motor protein in
870 homologous recombination. *Biochimica et Biophysica Acta (BBA) - Gene Regulatory Mechanisms*
871 **1809**, 509–523 (2011).

- 872 29. Mason, J. M. *et al.* RAD54 family translocases counter genotoxic effects of RAD51 in human
873 tumor cells. *Nucleic Acids Res* **43**, 3180–3196 (2015).
- 874 30. Holzen, T. M., Shah, P. P., Olivares, H. A. & Bishop, D. K. Tid1/Rdh54 promotes dissociation of
875 Dmc1 from nonrecombinogenic sites on meiotic chromatin. *Genes Dev.* **20**, 2593–2604 (2006).
- 876 31. Shah, P. P. *et al.* Swi2/Snf2-Related Translocases Prevent Accumulation of Toxic Rad51
877 Complexes during Mitotic Growth. *Molecular Cell* **39**, 862–872 (2010).
- 878 32. Li, X. & Heyer, W.-D. RAD54 controls access to the invading 3'-OH end after RAD51-mediated DNA
879 strand invasion in homologous recombination in *Saccharomyces cerevisiae*. *Nucleic Acids*
880 *Research* **37**, 638–646 (2009).
- 881 33. Wesoly, J. *et al.* Differential contributions of mammalian Rad54 paralogs to recombination, DNA
882 damage repair, and meiosis. *Mol Cell Biol* **26**, 976–989 (2006).
- 883 34. Russo, A., Cordelli, E., Salvitti, T., Palumbo, E. & Pacchierotti, F. Rad54/Rad54B deficiency is
884 associated to increased chromosome breakage in mouse spermatocytes. *Mutagenesis* **33**, 323–
885 332 (2018).
- 886 35. Liu, T., Wan, L., Wu, Y., Chen, J. & Huang, J. hSWS1-SWSAP1 Is an Evolutionarily Conserved
887 Complex Required for Efficient Homologous Recombination Repair *. *Journal of Biological*
888 *Chemistry* **286**, 41758–41766 (2011).
- 889 36. Prakash, R. *et al.* Distinct pathways of homologous recombination controlled by the SWS1–
890 SWSAP1–SPIDR complex. *Nat Commun* **12**, 4255 (2021).
- 891 37. Martino, J. *et al.* The human Shu complex functions with PDS5B and SPIDR to promote
892 homologous recombination. *Nucleic acids research* **47**, 10151–10165 (2019).
- 893 38. Godin, S. K. *et al.* Evolutionary and Functional Analysis of the Invariant SWIM Domain in the
894 Conserved Shu2/SWS1 Protein Family from *Saccharomyces cerevisiae* to *Homo sapiens*. *Genetics*
895 **199**, 1023–1033 (2015).
- 896 39. Martín, V. *et al.* Sws1 is a conserved regulator of homologous recombination in eukaryotic cells.
897 *The EMBO Journal* **25**, 2564–2574 (2006).

- 898 40. Abreu, C. M. *et al.* Shu complex SWS1-SWSAP1 promotes early steps in mouse meiotic
899 recombination. *Nat Commun* **9**, 3961 (2018).
- 900 41. Matsuzaki, K., Kondo, S., Ishikawa, T. & Shinohara, A. Human RAD51 paralogue SWSAP1 fosters
901 RAD51 filament by regulating the anti-recombinase FIGNL1 AAA+ ATPase. *Nat Commun* **10**, 1407
902 (2019).
- 903 42. Huang, T. *et al.* SPIDR is required for homologous recombination during mammalian meiosis.
904 *Nucleic Acids Research* gkad154 (2023) doi:10.1093/nar/gkad154.
- 905 43. Yuan, J. & Chen, J. FIGNL1-containing protein complex is required for efficient homologous
906 recombination repair. *Proc Natl Acad Sci U S A* **110**, 10640–10645 (2013).
- 907 44. Fernandes, J. B. *et al.* FIGL1 and its novel partner FLIP form a conserved complex that regulates
908 homologous recombination. *PLoS Genet* **14**, e1007317 (2018).
- 909 45. Zhang, P. *et al.* The Rice AAA-ATPase OsFIGNL1 Is Essential for Male Meiosis. *Frontiers in Plant*
910 *Science* **8**, (2017).
- 911 46. Liu, X. *et al.* OsRAD51 Plays a Vital Role in Promoting Homologous Recombination in Rice Meiosis.
912 *International Journal of Molecular Sciences* **23**, 9906 (2022).
- 913 47. Girard, C. *et al.* AAA-ATPase FIDGETIN-LIKE 1 and Helicase FANCM Antagonize Meiotic Crossovers
914 by Distinct Mechanisms. *PLOS Genetics* **11**, e1005369 (2015).
- 915 48. Hu, Q. *et al.* Meiotic Chromosome Association 1 Interacts with TOP3 α and Regulates Meiotic
916 Recombination in Rice. *The Plant Cell* **29**, 1697–1708 (2017).
- 917 49. Yang, S. *et al.* FIGNL1 Inhibits Non-homologous Chromosome Association and Crossover
918 Formation. *Frontiers in Plant Science* **13**, (2022).
- 919 50. Li, X. *et al.* Regulation of interference-sensitive crossover distribution ensures crossover
920 assurance in Arabidopsis. *Proc Natl Acad Sci U S A* **118**, e2107543118 (2021).
- 921 51. Kumar, R., Duhamel, M., Coutant, E., Ben-Nahia, E. & Mercier, R. Antagonism between BRCA2
922 and FIGL1 regulates homologous recombination. *Nucleic Acids Res* **47**, 5170–5180 (2019).

- 923 52. Sadate-Ngatchou, P. I., Payne, C. J., Dearth, A. T. & Braun, R. E. Cre recombinase activity specific
924 to post natal, premeiotic male germ cells in transgenic mice. *Genesis* **46**, 738–742 (2008).
- 925 53. Shi, B. *et al.* Dual functions for the ssDNA-binding protein RPA in meiotic recombination. *PLOS*
926 *Genetics* **15**, e1007952 (2019).
- 927 54. Imai, Y. *et al.* PRDM9 activity depends on HELLS and promotes local 5-hydroxymethylcytosine
928 enrichment. *Elife* **9**, e57117 (2020).
- 929 55. Bao, J., Ma, H.-Y., Schuster, A., Lin, Y.-M. & Yan, W. Incomplete cre-mediated excision leads to
930 phenotypic differences between Stra8-iCre; Mov10l1lox/lox and Stra8-iCre; Mov10l1lox/ Δ mice.
931 *genesis* **51**, 481–490 (2013).
- 932 56. Klein, H. L. The consequences of Rad51 overexpression for normal and tumor cells. *DNA Repair*
933 **7**, 686–693 (2008).
- 934 57. Baudat, F., Manova, K., Yuen, J. P., Jasin, M. & Keeney, S. Chromosome synapsis defects and
935 sexually dimorphic meiotic progression in mice lacking spo11. *Mol Cell* **6**, 989–998 (2000).
- 936 58. Romanienko, P. J. & Camerini-Otero, R. D. The mouse Spo11 gene is required for meiotic
937 chromosome synapsis. *Mol Cell* **6**, 975–987 (2000).
- 938 59. Pittman, D. L. *et al.* Meiotic prophase arrest with failure of chromosome synapsis in mice
939 deficient for Dmc1, a germline-specific RecA homolog. *Mol Cell* **1**, 697–705 (1998).
- 940 60. Yoshida, K. *et al.* The mouse RecA-like gene Dmc1 is required for homologous chromosome
941 synapsis during meiosis. *Mol Cell* **1**, 707–718 (1998).
- 942 61. Mahadevaiah, S. K. *et al.* Recombinational DNA double-strand breaks in mice precede synapsis.
943 *Nat Genet* **27**, 271-276. (2001).
- 944 62. Moens, P. B. *et al.* The time course and chromosomal localization of recombination-related
945 proteins at meiosis in the mouse are compatible with models that can resolve the early DNA-
946 DNA interactions without reciprocal recombination. *Journal of Cell Science* **115**, 1611–1622
947 (2002).

- 948 63. Yoon, S., Choi, E.-H., Kim, J.-W. & Kim, K. P. Structured illumination microscopy imaging reveals
949 localization of replication protein A between chromosome lateral elements during mammalian
950 meiosis. *Exp Mol Med* **50**, 1–12 (2018).
- 951 64. Yang, F. *et al.* Meiotic failure in male mice lacking an X-linked factor. *Genes Dev.* **22**, 682–691
952 (2008).
- 953 65. Wassing, I. E. & Esashi, F. RAD51: Beyond the break. *Semin Cell Dev Biol* **113**, 38–46 (2021).
- 954 66. Koornneef, L. *et al.* Multi-color dSTORM microscopy in Hormad1^{-/-} spermatocytes reveals
955 alterations in meiotic recombination intermediates and synaptonemal complex structure. *PLoS*
956 *Genetics* **18**, e1010046 (2022).
- 957 67. Carofiglio, F. *et al.* SPO11-independent DNA repair foci and their role in meiotic silencing. *PLoS*
958 *Genet* **9**, e1003538 (2013).
- 959 68. Khil, P. P., Smagulova, F., Brick, K. M., Camerini-Otero, R. D. & Petukhova, G. V. Sensitive mapping
960 of recombination hotspots using sequencing-based detection of ssDNA. *Genome Res* **22**, 957–
961 965 (2012).
- 962 69. Brick, K., Smagulova, F., Khil, P., Camerini-Otero, R. D. & Petukhova, G. V. Genetic recombination
963 is directed away from functional genomic elements in mice. *Nature* **485**, 642–645 (2012).
- 964 70. Lange, J. *et al.* The Landscape of Mouse Meiotic Double-Strand Break Formation, Processing, and
965 Repair. *Cell* **167**, 695-708.e16 (2016).
- 966 71. Davies, B. *et al.* Re-engineering the zinc fingers of PRDM9 reverses hybrid sterility in mice. *Nature*
967 **530**, 171–176 (2016).
- 968 72. Pittman, D. L., Weinberg, L. R. & Schimenti, J. C. Identification, characterization, and genetic
969 mapping of Rad51d, a new mouse and human RAD51/RecA-related gene. *Genomics* **49**, 103–111
970 (1998).
- 971 73. Mercier, R., Mézard, C., Jenczewski, E., Macaisne, N. & Grelon, M. The Molecular Biology of
972 Meiosis in Plants. *Annu. Rev. Plant Biol.* **66**, 297–327 (2015).

- 973 74. Petukhova, G. V., Romanienko, P. J. & Camerini-Otero, R. D. The Hop2 Protein Has a Direct Role
974 in Promoting Interhomolog Interactions during Mouse Meiosis. *Developmental Cell* **5**, 927–936
975 (2003).
- 976 75. Pezza, R. J., Petukhova, G. V., Ghirlando, R. & Camerini-Otero, R. D. Molecular activities of
977 meiosis-specific proteins Hop2, Mnd1, and the Hop2-Mnd1 complex. *J Biol Chem* **281**, 18426–
978 18434 (2006).
- 979 76. Zhao, W. & Sung, P. Significance of ligand interactions involving Hop2-Mnd1 and the RAD51 and
980 DMC1 recombinases in homologous DNA repair and XX ovarian dysgenesis. *Nucleic Acids*
981 *Research* **43**, 4055–4066 (2015).
- 982 77. Finsterbusch, F. *et al.* Alignment of Homologous Chromosomes and Effective Repair of
983 Programmed DNA Double-Strand Breaks during Mouse Meiosis Require the Minichromosome
984 Maintenance Domain Containing 2 (MCMDC2) Protein. *PLOS Genetics* **12**, e1006393 (2016).
- 985 78. McNairn, A. J., Rinaldi, V. D. & Schimenti, J. C. Repair of Meiotic DNA Breaks and Homolog Pairing
986 in Mouse Meiosis Requires a Minichromosome Maintenance (MCM) Paralog. *Genetics* **205**, 529–
987 537 (2017).
- 988 79. Lutzmann, M. *et al.* MCM8- and MCM9-deficient mice reveal gametogenesis defects and genome
989 instability due to impaired homologous recombination. *Mol Cell* **47**, 523–534 (2012).
- 990 80. Hustedt, N. *et al.* Control of homologous recombination by the HROB–MCM8–MCM9 pathway.
991 *Genes Dev.* **33**, 1397–1415 (2019).
- 992 81. Cole, F. *et al.* Mouse tetrad analysis provides insights into recombination mechanisms and
993 hotspot evolutionary dynamics. *Nat Genet* **46**, 1072–1080 (2014).
- 994 82. Piazza, A. & Heyer, W.-D. Moving forward one step back at a time: reversibility during
995 homologous recombination. *Curr Genet* **65**, 1333–1340 (2019).
- 996 83. Yu, D. S. *et al.* Dynamic Control of Rad51 Recombinase by Self-Association and Interaction with
997 BRCA2. *Molecular Cell* **12**, 1029–1041 (2003).

- 998 84. Lan, W.-H. *et al.* Rad51 facilitates filament assembly of meiosis-specific Dmc1 recombinase.
999 *Proceedings of the National Academy of Sciences* **117**, 11257–11264 (2020).
- 1000 85. Viera, A. *et al.* PDS5 proteins regulate the length of axial elements and telomere integrity during
1001 male mouse meiosis. *EMBO reports* **21**, e49273 (2020).
- 1002 86. Stok, C. *et al.* The FIGNL1-interacting protein C1orf112 is synthetic lethal with PICH and mediates
1003 RAD51 retention on chromatin. 2022.10.07.511242 Preprint at
1004 <https://doi.org/10.1101/2022.10.07.511242> (2022).
- 1005 87. Rinaldi, V. D., Bolcun-Filas, E., Kogo, H., Kurahashi, H. & Schimenti, J. C. The DNA Damage
1006 Checkpoint Eliminates Mouse Oocytes with Chromosome Synapsis Failure. *Mol Cell* **67**, 1026-
1007 1036.e2 (2017).
- 1008 88. Ravindranathan, R., Raveendran, K., Papanikos, F., San-Segundo, P. A. & Tóth, A. Chromosomal
1009 synapsis defects can trigger oocyte apoptosis without elevating numbers of persistent DNA
1010 breaks above wild-type levels. *Nucleic Acids Res* **50**, 5617–5634 (2022).
- 1011 89. Bolcun-Filas, E. *et al.* Mutation of the Mouse Syce1 Gene Disrupts Synapsis and Suggests a Link
1012 between Synaptonemal Complex Structural Components and DNA Repair. *PLOS Genetics* **5**,
1013 e1000393 (2009).
- 1014 90. Crichton, J. H., Dunce, J. M., Baarends, W. M., Davies, O. R. & Adams, I. R. Parallel recruitment
1015 pathways contribute to synaptonemal complex assembly during mammalian meiosis.
1016 2022.04.14.488335 Preprint at <https://doi.org/10.1101/2022.04.14.488335> (2022).
- 1017 91. Couturier, A. M. *et al.* Roles for APRIN (PDS5B) in homologous recombination and in ovarian
1018 cancer prediction. *Nucleic Acids Research* **44**, 10879–10897 (2016).
- 1019 92. Morales, C. *et al.* PDS5 proteins are required for proper cohesin dynamics and participate in
1020 replication fork protection. *Journal of Biological Chemistry* **295**, 146–157 (2020).
- 1021 93. Xu, H. *et al.* Molecular organization of mammalian meiotic chromosome axis revealed by
1022 expansion STORM microscopy. *Proceedings of the National Academy of Sciences* **116**, 18423–
1023 18428 (2019).

- 1024 94. Schwenk, F., Baron, U. & Rajewsky, K. A cre -transgenic mouse strain for the ubiquitous deletion
1025 of loxP -flanked gene segments including deletion in germ cells. *Nucleic Acids Research* **23**, 5080–
1026 5081 (1995).
- 1027 95. Abreu, C. M. *et al.* Shu complex SWS1-SWSAP1 promotes early steps in mouse meiotic
1028 recombination. *Nat Commun* **9**, 3961 (2018).
- 1029 96. Peters, A. H., Plug, A. W., van Vugt, M. J. & de Boer, P. A drying-down technique for the spreading
1030 of mammalian meiocytes from the male and female germline. *Chromosome research* **5**, 66–8
1031 (1997).
- 1032 97. Grey, C., Baudat, F. & Massy, B. de. Genome-Wide Control of the Distribution of Meiotic
1033 Recombination. *PLOS Biology* **7**, e1000035 (2009).
- 1034 98. Schindelin, J. *et al.* Fiji: an open-source platform for biological-image analysis. *Nat Methods* **9**,
1035 676–682 (2012).
- 1036 99. Lachmanovich, E. *et al.* Co-localization analysis of complex formation among membrane proteins
1037 by computerized fluorescence microscopy: application to immunofluorescence co-patching
1038 studies. *Journal of Microscopy* **212**, 122–131 (2003).
- 1039 100. Grey, C. *et al.* In vivo binding of PRDM9 reveals interactions with noncanonical genomic sites.
1040 *Genome research* **27**, 580–590 (2017).
- 1041 101. Brick, K., Pratto, F., Sun, C.-Y., Camerini-Otero, R. D. & Petukhova, G. Chapter Sixteen - Analysis
1042 of Meiotic Double-Strand Break Initiation in Mammals. in *Methods in Enzymology* (eds. Spies, M.
1043 & Malkova, A.) vol. 601 391–418 (Academic Press, 2018).
- 1044 102. Li, Q., Brown, J. B., Huang, H. & Bickel, P. J. Measuring reproducibility of high-throughput
1045 experiments. *The Annals of Applied Statistics* **5**, 1752–1779 (2011).
- 1046 103. Ramírez, F. *et al.* deepTools2: a next generation web server for deep-sequencing data analysis.
1047 *Nucleic Acids Research* **44**, W160–W165 (2016).

- 1048 104. Gomes, X. V., Henricksen, L. A. & Wold, M. S. Proteolytic mapping of human replication protein
1049 A: Evidence for multiple structural domains and a conformational change upon interaction with
1050 single-stranded DNA. *Biochemistry* **35**, 5586–5595 (1996).
- 1051 105. Veaute, X. *et al.* The Srs2 helicase prevents recombination by disrupting Rad51 nucleoprotein
1052 filaments. *Nature* **423**, 309–312 (2003).
- 1053 106. Dubochet, J., Ducommun, M., Zollinger, M. & Kellenberger, E. A new preparation method for
1054 dark-field electron microscopy of biomacromolecules. *Journal of ultrastructure research* **35**, 147–
1055 67 (1971).
- 1056
1057
1058
1059

1060

1061 **Supplementary Table 1. Primers used for mouse genotyping**

Primer	Sequence (5'-3')	Genotype: amplicon
<i>Firm</i> wild-type and floxed allele, forward	CTTGGCTCGCTTTGCTTTGA	WT: 304bp
<i>Firm</i> wild-type and floxed allele, reverse	TGTAGTTTACATCTTCCCTATGACA	<i>Firm^{fl}</i> : ~500bp <i>Firm⁻</i> : -
<i>Firm</i> floxed and deleted allele, forward	AAGGCGCATAACGATACCAC	WT: -
<i>Firm</i> floxed and deleted allele, reverse	ACTGATGGCGAGCTCAGACC	<i>Firm^{fl}</i> : ~1kb <i>Firm⁻</i> : 178bp
<i>Figl1</i> wild-type and floxed allele, forward	GGGATCAAACACTAGGGTTCAGGC	WT: 200bp
<i>Figl1</i> wild-type and floxed allele, reverse	GATACAGTCTTCAAGATTAAGGACAACC	<i>Figl1^{fl}</i> : 400bp <i>Figl1</i> : -
<i>Figl1</i> deleted allele, forward	GGGATCAAACACTAGGGTTCAGGC	WT: -
<i>Figl1</i> deleted allele, reverse	CGGGTTACGGTAGTTTACTCCC	<i>Figl1^{fl}</i> : - <i>Figl1</i> : 412bp
<i>Stra8-Cre</i> transgenic allele, forward	GTGCAAGCTGAACAACAGGA	No transgene: -
<i>Stra8-Cre</i> transgenic allele, reverse	AGGGACACAGCATTGGAGTC	<i>Stra8-Cre</i> : ~150bp
<i>Cmv-Cre</i> transgenic allele, forward	TGGGCGGCATGGTGCAAGTT	No transgene: -
<i>Cmv-Cre</i> transgenic allele, reverse	CGGTGCTAACCAGCGTTTTTC	<i>Cmv-Cre</i> : 466bp
<i>Spo11</i> wild-type and YF allele, forward	CTGGTCGATGCAGATCCCTACGG	WT: 394bp
<i>Spo11</i> wild-type and YF allele, reverse	TAGATGCACATTATCTCGATGCC	<i>Spo11^{YF}</i> : 482bp
<i>Swsap1</i> wild-type and deleted allele, forward	TCTGTGAAGTATAGCCAATGAGGC	WT: 396bp
<i>Swsap1</i> wild-type and deleted allele, reverse	AACTGTCACTCAGGCGGAACTAG	<i>Swsap1</i> : 265bp

1062

1063

1064

1065 **Supplementary Table 2. List of antibodies used in this study**

1066

Antibody	Source	Identifier/Reference	Application	Dilution
		DOI:		
Guinea-pig anti-SYCP3	home made	10.1371/journal.pbio.1000035	IF, WB	1:500, 1:3000
Mouse anti-SYCP3	Abcam	ab97672	IF	1:200
Rabbit anti-SYCP1	Abcam	ab15090	IF	1:400
Mouse anti- γ H2AX	Millipore	05-636-1	IF	1:10000
Guinea-pig anti-SYCP1	from H. Cook		IF	1:200
Rabbit anti-MSH4	Abcam	ab58666	IF	1:200
Rabbit anti-RPA2	Abcam	ab76420	IF	1:200
Rat anti-RPA2	Cell Signaling	2208	IF	1:200
Rabbit anti-DMC1	Santa Cruz	sc-22768	IF, WB	1:200, 1:1000
		DOI:		
Guinea-pig anti-DMC1	from Prof. Qinghua Shi	10.1016/j.molcel.2020.06.015	IF	1:100
Goat anti-DMC1	Santa Cruz	sc-8973	ChIP	
Rabbit anti-RAD51	Calbiochem	PC130	IF, WB	1:500, 1:1000
Rabbit anti-FIGNL1	Proteintech	17604-1-AP	WB	1:500
Rabbit anti-C1orf112 (anti-hFIRRM)	Abcam	ab121774	WB	1:500
Rabbit anti-beta Tubulin	Abcam	ab6046	WB	1:3000
Goat anti-rabbit A488	Molecular Probes	A-21206	IF	1:400
Goat anti-rabbit A555	Molecular Probes	A-21248	IF	1:400
Goat anti-rabbit Star Orange	Abberior GMBH	STORANGE-1002-5	IF -STED	1:100
Goat anti-guinea pig Cy3	Jackson	706-165-148	IF	1:400
Goat anti-guinea pig Cy5	Jackson	706-175-148	IF	1:400
Goat anti-guinea pig Star Red	Abberior GMBH	STRED-1006-500U	IF-STED	1:100
Donkey anti-rat A555	ThermoFisher	A48270	IF	1:400
Goat anti-rat Star Red	Abberior GMBH	STRED-1007-500U	IF-STED	1:100
Donkey anti-mouse A647	Thermo Fisher	ab150107	IF	1:400
Goat anti-mouse Star Green	Abberior GMBH	STGREEN-1001-50	IF-STED	1:100
Anti-rabbit HRP	Jackson Immunoresearch	711-035-152	WB	1:5000
Donkey anti-guinea pig HRP	Jackson Immunoresearch	706-035-148	WB	1:5000

1067

1068 IF, immunofluorescence; WB, western blotting; ChIP, chromatin immunoprecipitation

1069

1070

1071

1072

1073

1074 **Figure Legends**

1075

1076 **Figure 1a.** Testis weight relative to body weight in control (n=24), *Firrm* cKO (n=15), *Figl1* cKO (n=4)
1077 and *Firrm* cKO *Figl1* cKO (n=1) adult mice (30 dpp to 95 dpp). Unpaired t-test, two-sided. **b.** Periodic
1078 acid-Schiff-stained testis sections from adult mice of the indicated genotypes. Spg, spermatogonia;
1079 Spc, spermatocytes; rSpt, round spermatids; eSpt, elongated spermatids. Scale bar, 40 μ m. **c.** Western
1080 blot analysis of cytoplasmic (80 μ g) and nuclear (100 μ g) fractions from testes of 12 dpp mice of the
1081 indicated genotypes. **d.** Chromosome axes (SYCP3, red) and synaptonemal complex (SYCP1, green)
1082 were detected in spread leptotene, early zygotene (control) or zygotene-like (cKO), and pachytene
1083 (control) or late zygotene-like (cKO) spermatocyte nuclei from control, *Firrm* cKO and *Figl1* cKO mice.
1084 Scale bar, 10 μ m. **e.** Distribution of spermatocytes at different meiotic prophase substages in juvenile
1085 *Firrm* cKO mice (indicated age) and in adult (8-week-old) *Figl1* cKO mice. Chi-square test. For all
1086 figures: ns, non-significant; *0.01 < p \leq 0.05; **0.001 < p \leq 0.01; ***0.0001 < p \leq 0.001; ****p \leq 0.0001.

1087

1088 **Figure 2. Early recombination events are normal in *Firrm* cKO and *Figl1* cKO spermatocytes.**

1089 **a.** Representative images of spread nuclei of pre-leptotene, early leptotene and leptotene
1090 spermatocytes from control and *Firrm* cKO mice stained for SYCP3 and γ H2AX. Scale bar, 20 μ m. **b.**
1091 Total nuclear γ H2AX signal intensity in control (gray) and *Firrm* cKO (red) spermatocytes (n=2 mice per
1092 genotype). **c.** Representative images of spread spermatocyte nuclei from 12 dpp control and *Firrm*
1093 cKO mice stained for SYCP3 and RPA2. Scale bar, 10 μ m. **d.** Number of on-axis RPA2 foci in control
1094 (gray), *Firrm* cKO (red) and *Figl1* cKO (orange) spermatocytes. Mann-Whitney two-tailed test; n=5
1095 (control), n=4 (*Firrm* cKO) and n=2 (*Figl1* cKO) mice per genotype.

1096

1097 **Figure 3. *Firrm* cKO and *Figl1* cKO spermatocytes accumulate RAD51 and DMC1, and are deficient**

1098 **for later meiotic HR intermediates.** **a.** Representative images of zygotene spermatocyte spreads from
1099 control and *Firrm* cKO mice stained for SYCP3, RAD51 and DMC1. Scale bar, 5 μ m. **b, c.** Numbers of
1100 RAD51 (**b**) and DMC1 (**c**) foci in control and *Firrm* cKO (**b**), and in control, *Firrm* cKO and *Figl1* cKO
1101 spermatocytes (**c**). n=2 mice per genotype, except for RAD51 foci in *Figl1* cKO (n=1). **d.** Representative
1102 spreads of zygotene spermatocytes from 16 dpp control, *Firrm* cKO and *Spo11*^{YF/YF} mice stained with
1103 SYCP3, SYCP1 and MSH4. Scale bar, 10 μ m. **e.** MSH4 focus density along SYCP1-marked synaptonemal
1104 complex fragments in control, *Firrm* cKO, *Spo11*^{YF/YF} *Firrm* cKO, and *Spo11*^{YF/YF} zygotene/zygotene-like
1105 spermatocytes. Mann-Whitney two-tailed test. n=3 mice per genotype. **f.** Preleptotene spermatocyte
1106 spreads from control and *Firrm* cKO mice stained for SYCP3, RPA2 (red) and RAD51 (green). Scale bar,
1107 10 μ m. **g.** STED images of preleptotene spermatocyte spreads from control and *Firrm* cKO mice stained

1108 for RAD51 (STAR ORANGE, green) and RPA2 (STAR RED, red). Scale bar, 1 μ m. **h-i.** Number of RAD51
1109 foci that colocalized with RPA2 foci (**h**) and of RPA2 foci that colocalized with RAD51 (**i**) in spreads of
1110 preleptotene control and *Fignl1* cKO spermatocyte nuclei (n=1 mouse per genotype). The observed
1111 (obs) and expected by chance (random) numbers of colocalized foci are shown. Mann-Whitney two-
1112 tailed test.

1113

1114 **Figure 4. RAD51 and DMC1 patterns in mouse meiotic chromosomes. a-c.** Number (**a**) of on-axis
1115 RAD51 foci that colocalized with on-axis DMC1 foci, and vice-versa, in spreads from control and *Firrm*
1116 cKO spermatocytes from 12 dpp mice. The observed (obs) and expected by chance (random) numbers
1117 of RAD51 foci that colocalized with DMC1 are shown in (**a**). Random, average of 100 simulations where
1118 the colocalization of randomly distributed DMC1 foci with actual RPA2 foci was measured. Wilcoxon
1119 two-tailed test. **b,c.** Percentage (corrected for random colocalization, see Methods) of on-axis RAD51
1120 foci colocalized with on-axis DMC1 foci (**b**) and vice-versa (**c**). There were not enough on-axis RAD51
1121 and DMC1 foci in early leptotene control spermatocytes to measure colocalization reliably. Mann-
1122 Whitney two-tailed test. **d.** STED images of spreads of leptotene spermatocyte nuclei stained for SYCP3
1123 (STAR GREEN, white), RAD51 (STAR ORANGE, green), and DMC1 (STAR RED, red). **e.** STED images of
1124 spreads of zygotene/zygotene-like spermatocyte nuclei with extensive synaptonemal complexes,
1125 stained for SYCP3 (STAR 460L, white), RAD51 (STAR RED, red) and DMC1 (STAR ORANGE, green). **f.**
1126 Relative intensity of SYCP3 (black), RAD51 (red) and DMC1 (green) signal across the synaptonemal
1127 complex in control (across RAD51-DMC1 mixed foci) and *Firrm* cKO (outside regions of stronger focus-
1128 like RAD51-DMC1 staining). Data are the mean of 12 sections from STED images of 3 different nuclei.

1129

1130 **Figure 5. FIRRM prevents DSB-independent accumulation of RAD51 and DMC1 in mouse**
1131 **spermatocyte chromosomes. a.** Spreads of representative control, *Firrm* cKO, *Spo11^{YF/YF}* *Firrm* cKO,
1132 and *Spo11^{YF/YF}* early zygotene spermatocytes stained for SYCP3, DMC1 and RAD51. Scale bar, 10 μ m.
1133 **b-c.** Counts of on-axis RAD51 (**b**) and DMC1 (**c**) foci in spreads from control, *Firrm* cKO, *Spo11^{YF/YF}* *Firrm*
1134 cKO, and *Spo11^{YF/YF}* spermatocytes from 12 dpp mice. Foci overlapping with (on-axis, top panels) or
1135 outside (Extended Data Figure 4c-d) chromosome axes, defined by the SYCP3 signal, were counted
1136 separately. Mann-Whitney two-tailed test. n=2 mice per genotype.

1137

1138 **Figure 6. DMC1 is recruited at meiotic DSB hotspots in *Firrm* cKO spermatocytes. a-b.** Percentages of
1139 on-axis RPA2 foci colocalized with on-axis DMC1 foci (**a**), and of DMC1 foci colocalized with RPA2 (**b**)
1140 in spreads from early leptotene to mid-zygotene/zygotene-like spermatocyte nuclei from control and
1141 *Firrm* cKO mice. Mann-Whitney two-tailed test. **c.** Numbers of and shared hotspots identified by
1142 DMC1-SSDS in spermatocytes from 12 dpp control and *Firrm* cKO mice. **d.** DMC1-SSDS signal

1143 correlation between control and *Firrm* cKO mice at hotspots identified in both genotypes. The
1144 Spearman rho and associated p-value (two-sided) are shown. Red and green dots indicate hotspots
1145 that were significantly over- and under-represented in *Firrm* cKO compared with control
1146 spermatocytes (DESeq2, p-value <0.1, log2FC >0 and log2FC <0, respectively). Unchanged autosomal
1147 hotspots are represented in gray and chromosome X hotspots by black circled diamonds. **e.** Average
1148 plots (top) and corresponding heatmaps (bottom) of DMC1-SSDS intensity (fragments per million,
1149 FPM) in control (left) and *Firrm* cKO mice (right) for hotspots that overlap with SPO11-oligo hotspots
1150 ⁷⁰ detected in both genotypes (common peaks), in control only (control-specific), or in *Firrm* cKO only
1151 (*Firrm* cKO-specific)(see Extended Data Fig. 7a). The center of intervals is defined as the center of
1152 SPO11-oligo peaks detected in B6 mice, as defined in (Lange, 2016). **f.** Normalized average distribution
1153 of ssDNA type 1 fragments (see Methods) originating from forward (fwd) and reverse strands (rev) at
1154 common peaks, defined in (**e**), for control (red, orange) and *Firrm* cKO (blue, light blue). The SSDS signal
1155 was normalized to have the same cumulated amount of normalized signal from both forward and
1156 reverse strands over common peaks (on 5-kb windows) for both genotypes.

1157

1158 **Figure 7. *Firrm* and *Figl1* deletion restore RAD51 and DMC1 loading in *Swsap1*^{-/-} spermatocytes. **a.****
1159 **Spreads of control, *Firrm* cKO, *Swsap1*^{-/-} *Firrm* cKO, and *Swsap1*^{-/-} early zygotene spermatocytes stained**
1160 **for SYCP3 (gray), RAD51 (yellow) and RPA2 (magenta). Scale bar, 10 μm. **b-d.** Numbers of on-axis RPA2**
1161 **(**b**), RAD51 (**c**) and DMC1 (**d**) foci in spreads from control, *Figl1* cKO, and *Swsap1*^{-/-} *Figl1* cKO**
1162 **spermatocytes from 17 dpp mice. Mann-Whitney two-tailed test. n=1 mouse per genotype. **e-f.****
1163 **Percentage of on-axis RPA2 foci colocalized with on-axis RAD51 (**e**) or DMC1 (**f**) foci on spreads from**
1164 **control, *Figl1* cKO, and *Swsap1*^{-/-} *Figl1* cKO spermatocytes from 17dpp mice. The numbers of**
1165 **colocalized foci were corrected for the numbers expected by chance (see Methods).**

1166

1167 **Figure 8. FIGLN1 alters the architecture and the activity of RAD51 and DMC1 nucleoprotein**
1168 **filaments. **a-b.** Electrophoretic Mobility Shift Assay (EMSA). 1 μM RAD51 or DMC1 was incubated (20**
1169 **minutes) with 3 μM (nucleotide concentration) of a Cy5-labeled 400 nt ssDNA fragment (**a**) or a Cy5-**
1170 **labeled 200 bp dsDNA fragment (**b**) with or without 1.6 μM human FIGNL1ΔN. For the pre-formed**
1171 **nucleofilament panels, RAD51 or DMC1 was incubated with DNA for 5 minutes before adding**
1172 **FIGNL1ΔN for 15 minutes. For the no pre-formed filament panels, RAD51 or DMC1 was added to the**
1173 **reaction concomitantly with FIGNL1ΔN. **c.** Quantification of free dsDNA in the EMSA performed with**
1174 **dsDNA and without pre-formed nucleofilament shown in (**b**). n=2 per condition. Paired t-test, two-**
1175 **sided. **d-f.** Representative TEM images in positive (**d**) and negative staining (**e**) and length distribution**
1176 **(**f**) of RAD51 filaments assembled on 400 nt ssDNA fragments (ss400) without (left, ss400-RAD51) or**
1177 **with human FIGNL1ΔN (right, ss400-RAD51 + FIGNL1ΔN). Some very long filaments (>450nm) that**

1178 formed in the presence of FIGNL1ΔN **(d)** were not included in the quantification in **(f)** (see Extended
1179 Data Fig. 9b). **g-h.** FIGNL1ΔN inhibits the formation of a D-loop by RAD51 and DMC1 *in vitro*.
1180 Representative gel (RAD51 in the presence of increasing concentrations of FIGNL1ΔN, from 0.4 to 1.6
1181 μM) **(g)**. Titration of FIGNL1ΔN **(h)** in the D-loop assay. **i.** Model for possible (and non-exclusive) roles
1182 of the FIGNL1-FIRRM complex in regulating RAD51 and DMC1 in mouse spermatocytes. (i) The FIGNL1-
1183 FIRRM complex may limit the nuclear RAD51 level by sequestering a cytoplasmic RAD51 pool, possibly
1184 by promoting RAD51 polymerization, thus preventing its mobilization by BRCA2. (ii) The FIGNL1-FIRRM
1185 complex might prevent the stabilization of transient dsDNA-RAD51 association at replication forks
1186 during premeiotic replication. (iii) During meiotic recombination, the FIGNL1-FIRRM complex might
1187 first promote indirectly the polymerization of a continuous DMC1 filament on the meiotic DSB 3' ssDNA
1188 overhang by preventing the loading of stable RAD51 patches on the 3' region of the ssDNA tails. This
1189 would allow the 5' to 3' polymerization of DMC1 (arrows) up to the 3' ends. A factor (e.g., the SWSAP1-
1190 SWS1-SPIDR complex) may protect the RAD51 filament from FIGNL1-FIRRM-dependent dissociation in
1191 the dsDNA-proximal region of ssDNA tails. The formation of shorter/patchy DMC1 filaments in the
1192 absence of the FIGL1-FIRRM complex might not be fully functional for homology search, strand
1193 invasion and D-loop stabilization. Post-strand invasion, the FIGNL1-FLIP complex might also be involved
1194 in removing RAD51/DMC1 from invading ends involved in intersister (not shown) and/or interhomolog
1195 interactions.

1196
1197 **Extended Fig. 1. Structure of *Firrm* and *Figl1* cKO alleles.** **a.** Genomic structure of the floxed and
1198 knockout (KO) *Firrm* and *Figl1* alleles. Open boxes, coding exons; gray-filled boxes, non-coding exons.
1199 **b.** The mouse FIRRM protein. The conserved DUF4487 domain is indicated, with the position of exon
1200 7 deleted in the KO (generating a frameshift), and the following internal methionine (M, position 406).

1201
1202 **Extended Fig. 2. Increased RAD51 and DMC1 loading, and defective MSH4 and TEX11 focus**
1203 **formation, in *Firrm* cKO and *Figl1* cKO spermatocytes.** **a.** Representative images of pre-leptotene to
1204 late zygotene spermatocyte spreads from control and *Firrm* cKO mice stained for SYCP3, RAD51 and
1205 DMC1. Scale bar, 10 μm. **2b.** Spreads of zygotene spermatocytes from 16 dpp control and *Firrm* cKO
1206 mice stained with SYCP3 and TEX11. **c.** Number of MSH4 foci along SYCP1-marked synaptonemal
1207 complex fragments in control, *Firrm* cKO, *Spo11*^{YF/YF} *Firrm* cKO, and *Spo11*^{YF/YF} zygotene or zygotene-
1208 like spermatocytes. The number of MSH4 foci varied with the SC length in control and *Firrm* cKO
1209 spermatocytes. The linear regression fit is shown, with the standard error. **d.** Numbers of off-axis RPA2
1210 foci in control (gray), *Firrm* cKO and *Figl1* cKO spermatocytes (red). Mann-Whitney two-tailed test.
1211 n=3 (control) and n=2 (*Firrm* cKO and *Figl1* cKO) mice per genotype. **e.** Numbers of all and of
1212 colocalized RAD51 (green) and RPA2 (red) foci in spreads of preleptotene control and *Figl1* cKO

1213 spermatocyte nuclei (n=1 mouse per genotype). The numbers of colocalized foci were corrected for
1214 the number of colocalized foci expected by chance (see Methods). Mann-Whitney two-tailed test.

1215

1216 **Extended Fig. 3. Colocalization of on- and off-axis DMC1 and RAD51 foci in *Firrm* cKO spermatocytes.**

1217 **a.** Number of on-axis DMC1 foci colocalized with on-axis RAD51 foci from early leptotene to mid-
1218 zygotene/zygotene-like stage in control and *Firrm* cKO spread spermatocyte nuclei from 12 dpp mice.
1219 The observed (obs) and expected by chance (random) numbers of RAD51 foci colocalized with DMC1
1220 are shown. obs, number of detected colocalized foci. Random, average of 100 simulations where the
1221 colocalization of randomly distributed RAD51 foci with actual RPA2 foci was measured. Wilcoxon two-
1222 tailed test. **b, c.** Number of off-axis RAD51 foci colocalized with off-axis DMC1 foci (**b**) and number of
1223 off-axis DMC1 foci colocalized with off-axis RAD51 foci (**c**) from preleptotene to mid-
1224 zygotene/zygotene-like in spread spermatocyte nuclei from 12 dpp control and *Firrm* cKO mice. **d, e.**
1225 Percentage of RAD51 foci colocalized with DMC1 (**d**), and of DMC1 foci colocalized with RAD51 (**e**),
1226 corrected for random colocalization. Mann-Whitney two-tailed test.

1227

1228 **Extended Fig. 4. Meiotic DSBs do not form in *Spo11*^{YF/YF} *Firrm* cKO spermatocytes.** Representative
1229 spread nuclei of spermatocytes from control, *Firrm* cKO, *Spo11*^{YF/YF} *Firrm* cKO, and *Spo11*^{YF/YF} mice
1230 stained for SYCP3, SYCP1 and γ H2AX (**a**) or for SYCP3 and RPA2 (**b**). Scale bar, 10 μ m.

1231

1232 **Extended Fig. 5. SPO11 DSB-independent DMC1 and RAD51 foci colocalize in *Spo11*^{YF/YF} *Firrm* cKO**
1233 **spermatocytes. a-f.** Numbers of off-axis RAD51 (**a**) and DMC1 (**b**) foci for control, *Firrm* cKO, *Spo11*^{YF/YF}
1234 *Firrm* cKO, and *Spo11*^{YF/YF} spermatocyte spreads. n=2 mice per genotype. Mann-Whitney two-tailed
1235 test **c-f.** Number (**c-d**) and percentage (corrected for random colocalization) (**e-f**), of on-axis RAD51
1236 foci colocalized with on-axis DMC1 foci (**c,e**) and vice-versa (**d,f**), from early leptotene to mid-
1237 zygotene/zygotene-like on spread from spermatocytes of 12 dpp control, *Firrm* cKO, *Spo11*^{YF/YF} *Firrm*
1238 cKO, and *Spo11*^{YF/YF} mice. n=2 mice per genotype.

1239

1240 **Extended Fig. 6. Similar numbers of DMC1 and RPA foci colocalize in wild-type and *Firrm* cKO**
1241 **spermatocytes. a-b.** Number of on-axis DMC1 foci colocalized with on-axis RPA2 foci on spreads from
1242 early leptotene to mid-zygotene/zygotene-like spermatocyte nuclei from control and *Firrm* cKO mice.
1243 The observed (obs) and expected by chance (random) numbers of DMC1 foci colocalized with RPA2
1244 are shown in (**a**), while the counts are corrected for the number expected by chance in (**b**). obs, number
1245 of detected colocalizing foci. Random, average of 100 simulations where the colocalization of randomly
1246 distributed DMC1 foci with actual RPA2 foci was measured. Wilcoxon two-tailed test (**a**). Mann-
1247 Whitney two-tailed test (**b**). **c-f.** Number (**c-d**) and percentages (**e-f**) of on-axis DMC1 foci colocalized

1248 with on-axis RPA2 foci on spreads from early leptotene to mid-zygotene/zygotene-like spermatocyte
1249 nuclei from control and *Figl1* cKO mice. The observed (obs) and expected by chance (random) counts
1250 of DMC1 foci colocalized with RPA2 are shown in (c), while the counts were corrected for the number
1251 expected by chance in (d). obs, number of observed colocalizing foci. Random, average of 100
1252 simulations where the colocalization of randomly distributed on-axis DMC1 foci with actual on-axis
1253 RPA2 foci was measured. Wilcoxon two-tailed test. e, f. Percentage (corrected for random
1254 colocalization) of DMC1 foci colocalized with RPA2 (e), and of RPA2 foci colocalized with DMC1 (f).
1255 Mann-Whitney two-tailed test.

1256

1257 **Extended Fig. 7. DMC1 recruitment at meiotic DSB hotspots in *Firrm* cKO spermatocytes.** a. Numbers
1258 and overlap of hotspots identified by DMC1-SSDS in spermatocytes from 12 dpp control and *Firrm* cKO
1259 mice, and of SPO11-oligo hotspots detected in C57BL/6J mice in ⁷⁰. b-c. Average plots (top) and
1260 corresponding heatmaps (bottom) of DMC1-SSDS signal in control and *Firrm* cKO mice (2 biological
1261 replicates/each), at all common, control-specific, and *Firrm* cKO-specific DMC1 hotspots identified in
1262 our analysis (b), and at hotspots overlapping with SPO11-oligo hotspots detected in C57BL/6J mice (c).
1263 In (c), the center of the intervals was the center of SPO11-oligo peaks detected in B6 mice, as defined
1264 in (Lange, 2016). d. Average DMC1-SSDS signal distribution at common DMC1 hotspots, defined in (c),
1265 at autosomal hotspots (left panel) and at X and Y chromosome hotspots (right panel), for control (blue)
1266 and *Firrm* cKO (red). The DMC1-SSDS signal was normalized to have the same total amount of
1267 normalized signal for all common hotspots (on 5-kb windows) in both genotypes. The relative excess
1268 of DMC1-SSDS signal at X-Y chromosome hotspots in control is clear. e. Average plots of DMC1-SSDS
1269 signal intensity (in FPM) at common hotspots defined in (c), ranked within 5 bins of decreasing
1270 intensity.

1271

1272 **Extended Fig. 8. *Figl1* deletion restores the formation of RAD51 and DMC1 loading in *Swsap1*^{-/-}**
1273 **spermatocytes.** a-c. Numbers of off-axis RPA2 (a), RAD51 (b) and DMC1 (c) foci detected on
1274 spermatocyte spreads from 17 dpp control, *Figl1* cKO, and *Swsap1*^{-/-} *Figl1* cKO mice. Mann-Whitney
1275 two-tailed test. n=1 mouse per genotype. d-g. Numbers (d-e) or percentages (f-g) of on-axis RAD51
1276 (d,f), and DMC1 (e,g) foci colocalized with on-axis RPA2 foci in spermatocyte spreads from 17 dpp
1277 control, *Figl1* cKO, and *Swsap1*^{-/-} *Figl1* cKO mice. The numbers of colocalized foci were corrected to
1278 the number expected by chance (see Methods). Mann-Whitney two-tailed test. n=1 mouse per
1279 genotype.

1280

1281 **Extended Fig. 9. FIGLN1 alters the architecture and the activity of RAD51 and DMC1 nucleoprotein**
1282 **filaments.** a. Purification of recombinant Histidine-tagged human FIGLN1ΔN284 protein from *E. coli*.

1283 Top panel, SDS-page analysis of proteins in total protein lysate (L), soluble protein fraction (S), flow-
1284 through (FT) from Hi-trap column, wash, and elution fractions (E1 to E7). Bottom panel, SDS-PAGE
1285 analysis of protein fractions collected during the gel filtration purification. Fractions E3, E4, and E5
1286 from previous step were pooled and are shown as input control. Red arrows indicate recombinant His-
1287 FIGNL1 Δ N284 with an expected size of 46kDa. F11 and F12 fractions were used for biochemical assays
1288 in this study. **b.** Length distribution of RAD51 filaments formed on 400 nt ssDNA fragments without
1289 (ss400-RAD51) or with (ss400-RAD51+ FIGNL1 Δ N) 1.6 μ M human FIGNL1 Δ N. Note the presence of
1290 >450nm-long filaments when FIGNL1 Δ N is present that were not included in the quantification shown
1291 in Figure 8f. **c.** Representative TEM images of RAD51 in the presence of ATP but in the absence of DNA
1292 (negative staining, left), and in presence of human FIGNL1 Δ N (negative staining, scale bar 100nm, top
1293 right panel; and positive staining, scale bar 500nm, bottom panel). Note the presence of long filaments
1294 despite the absence of DNA. **d.** Representative TEM images (negative staining) of DMC1 filaments
1295 assembled on a 400 bp dsDNA (top) or 400 nt ssDNA (bottom) fragment, without (left) or with human
1296 FIGNL1 Δ N (right). Scale bar, 100 nm.

1297

1298 **Source Data. a-b.** Uncropped image of the gels shown in Fig. 8a-b. Unlabeled lanes are not displayed
1299 on the final figure.

Figure 1

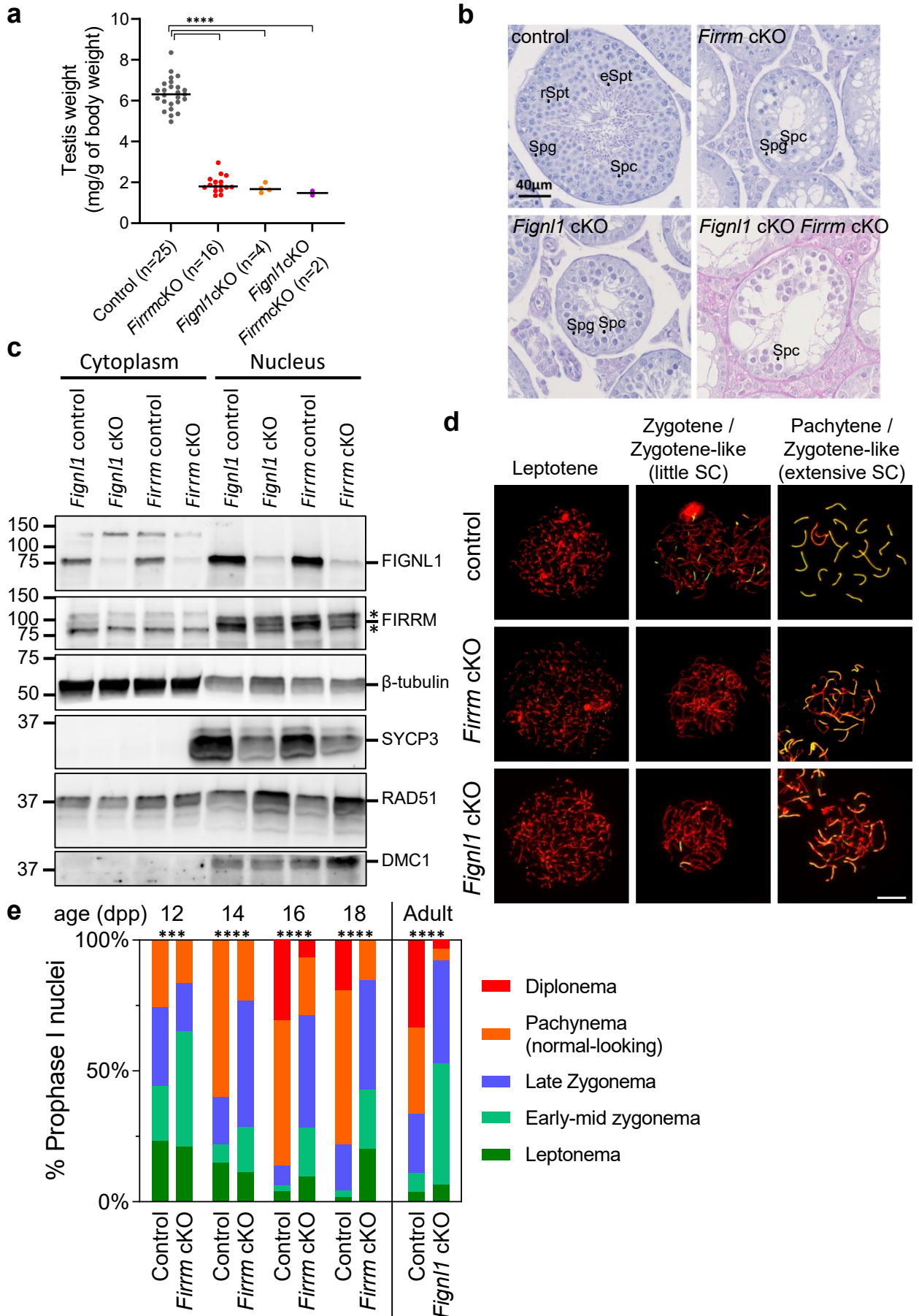


Figure 2

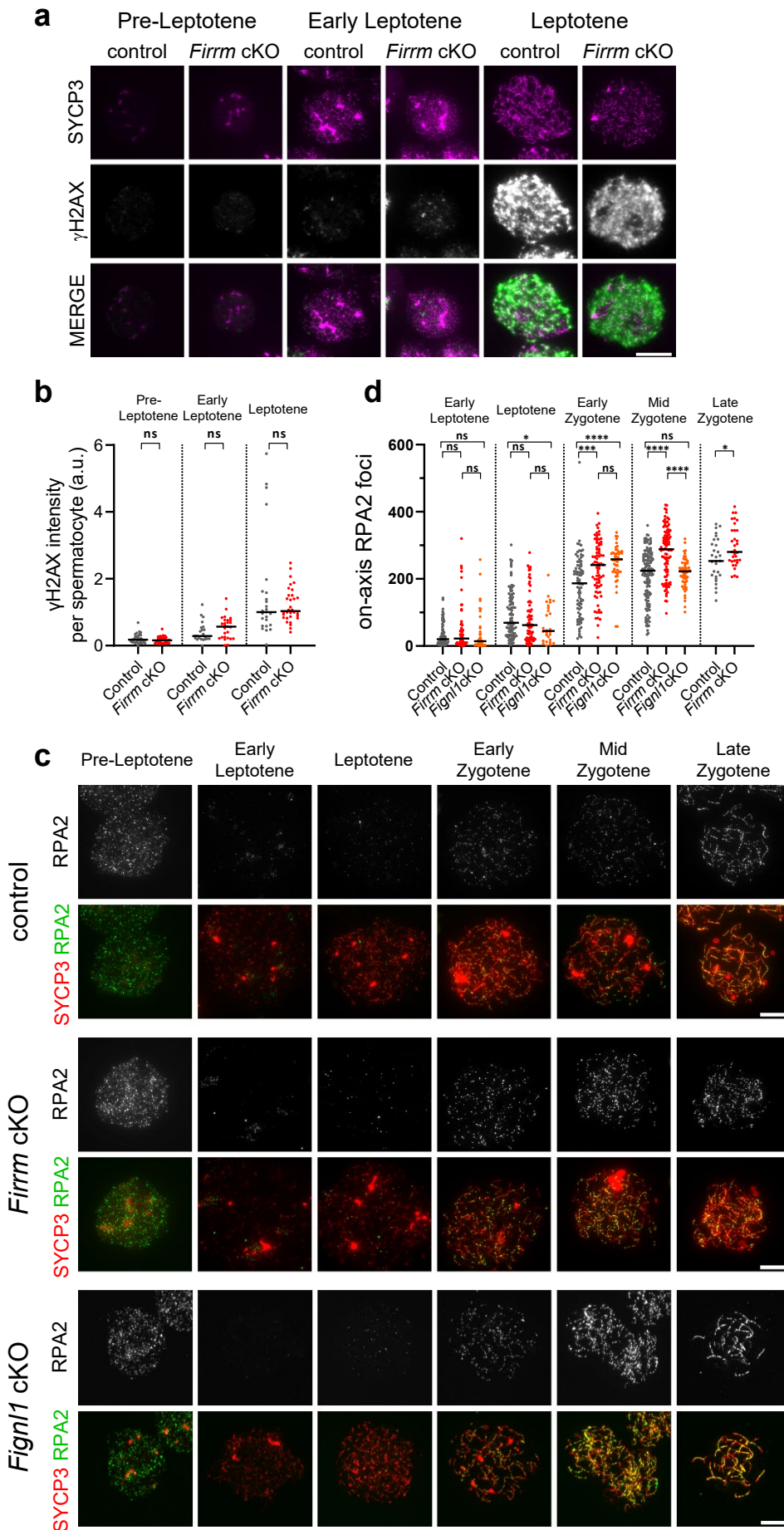


Figure 3

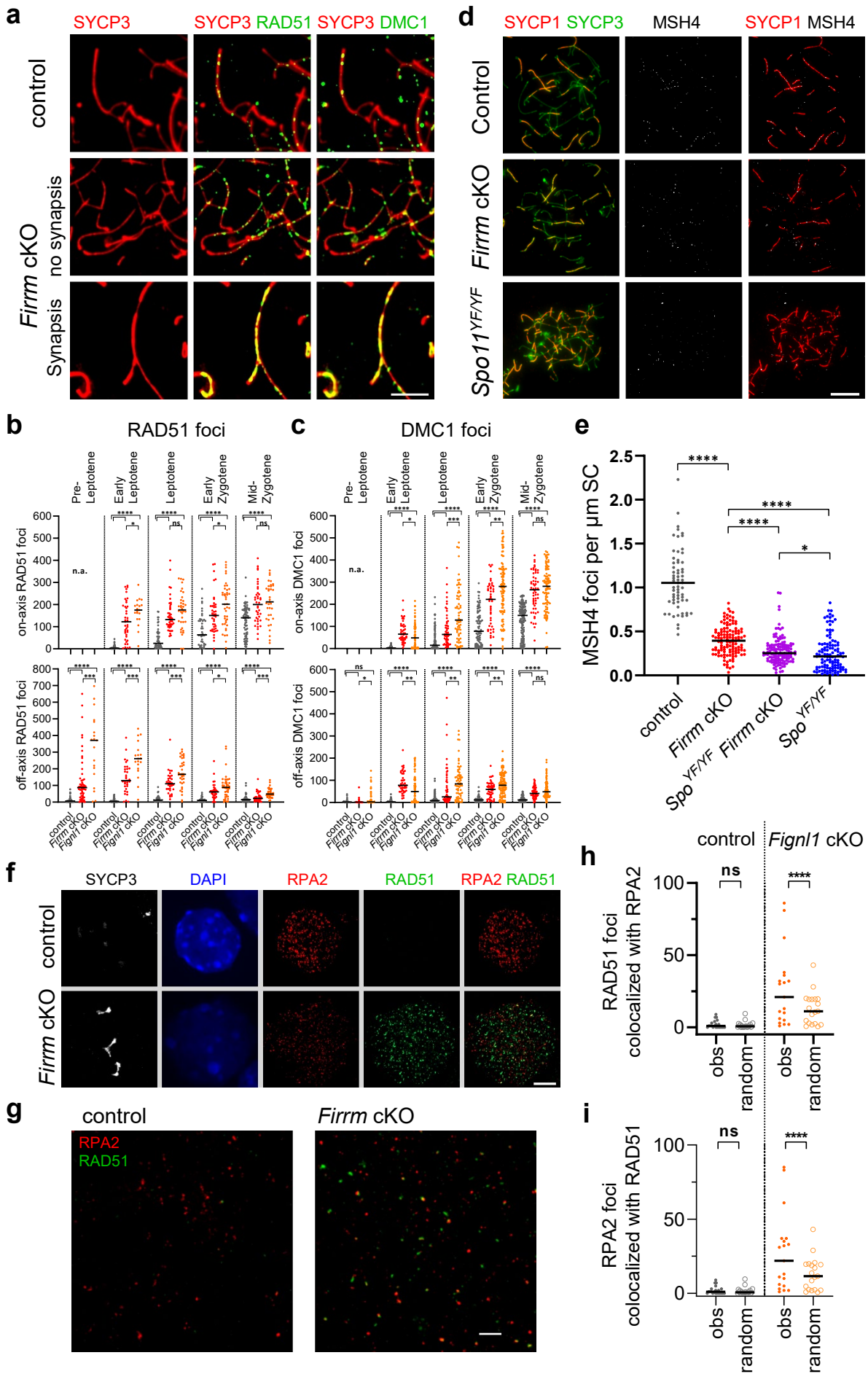


Figure 4

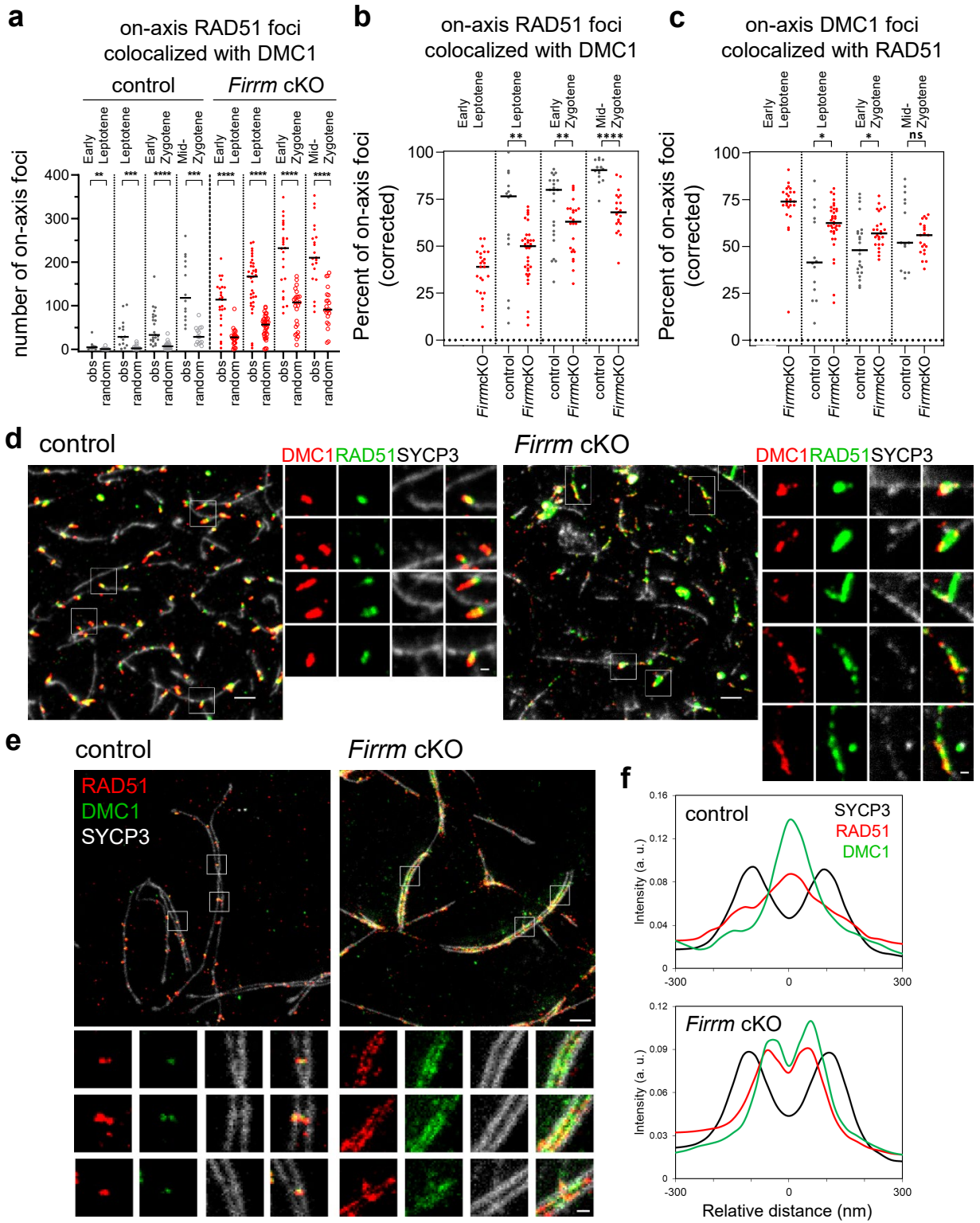


Figure 5

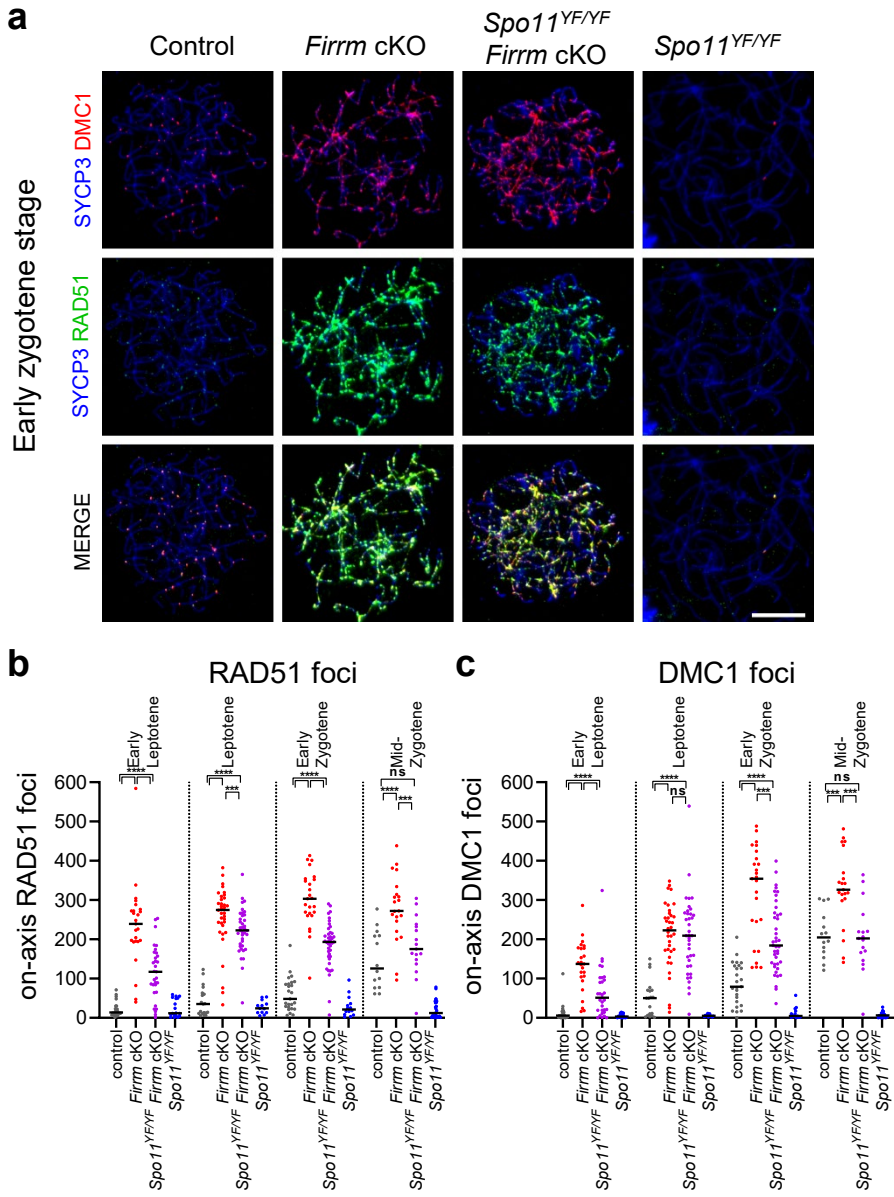


Figure 6

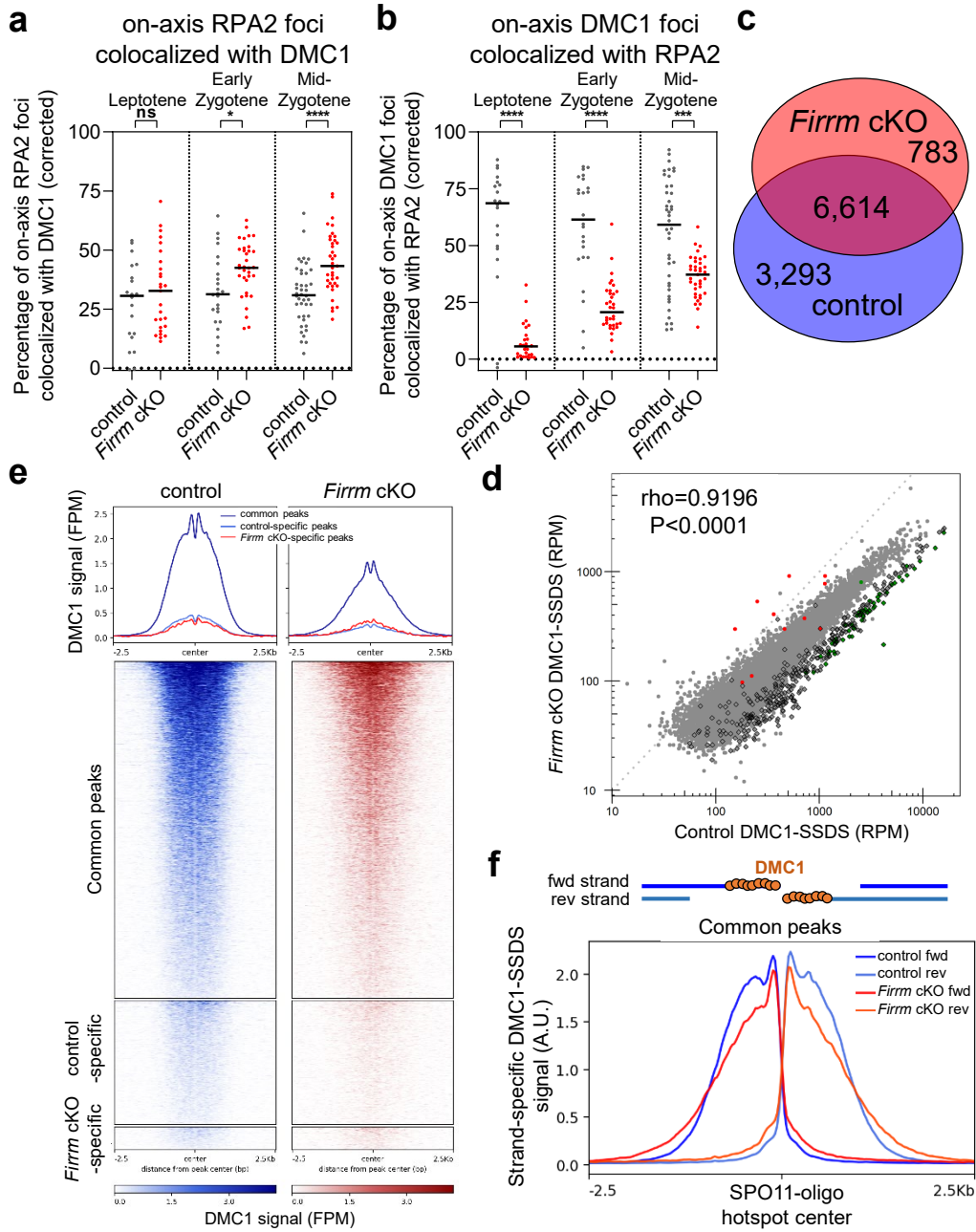


Figure 7

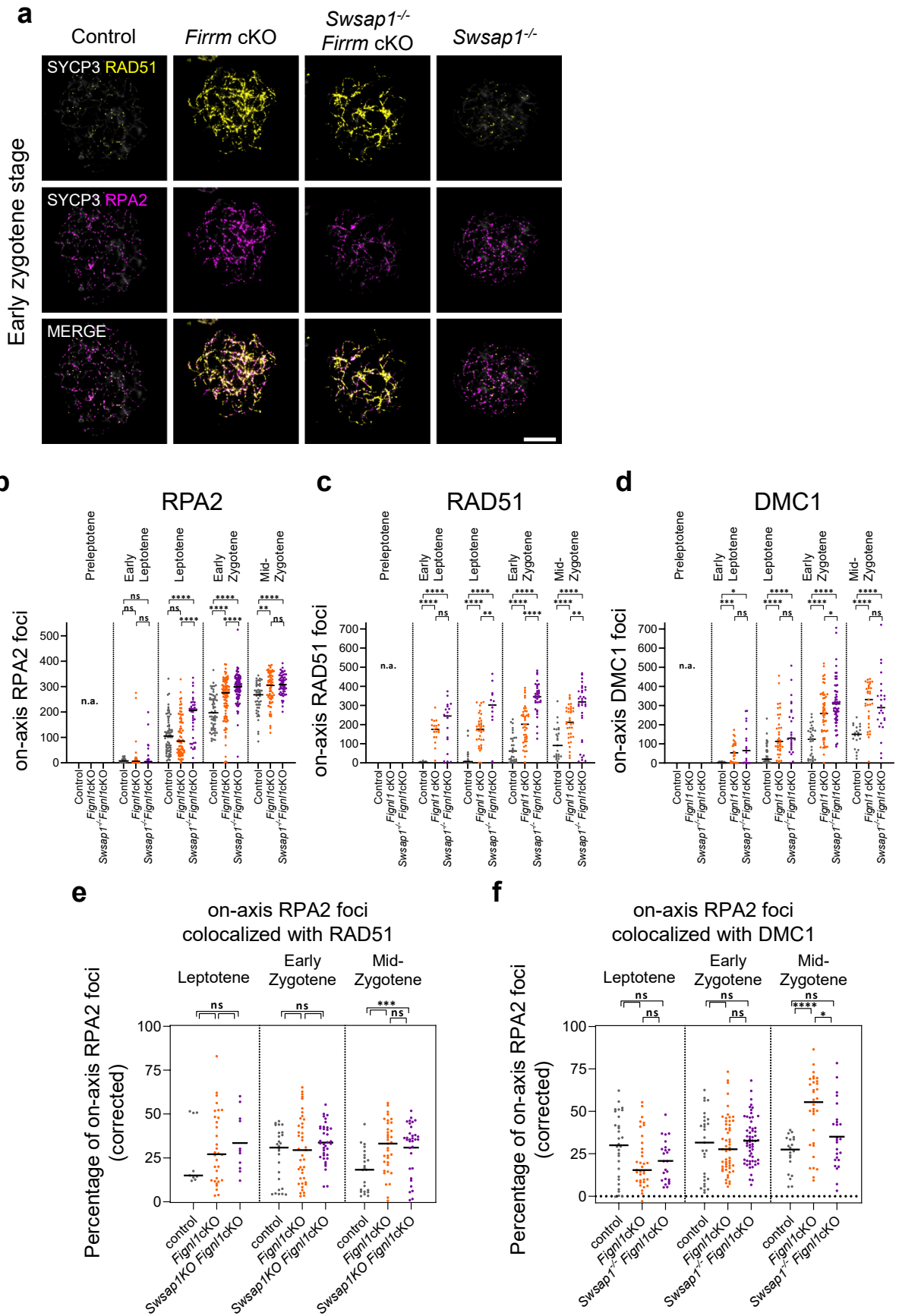
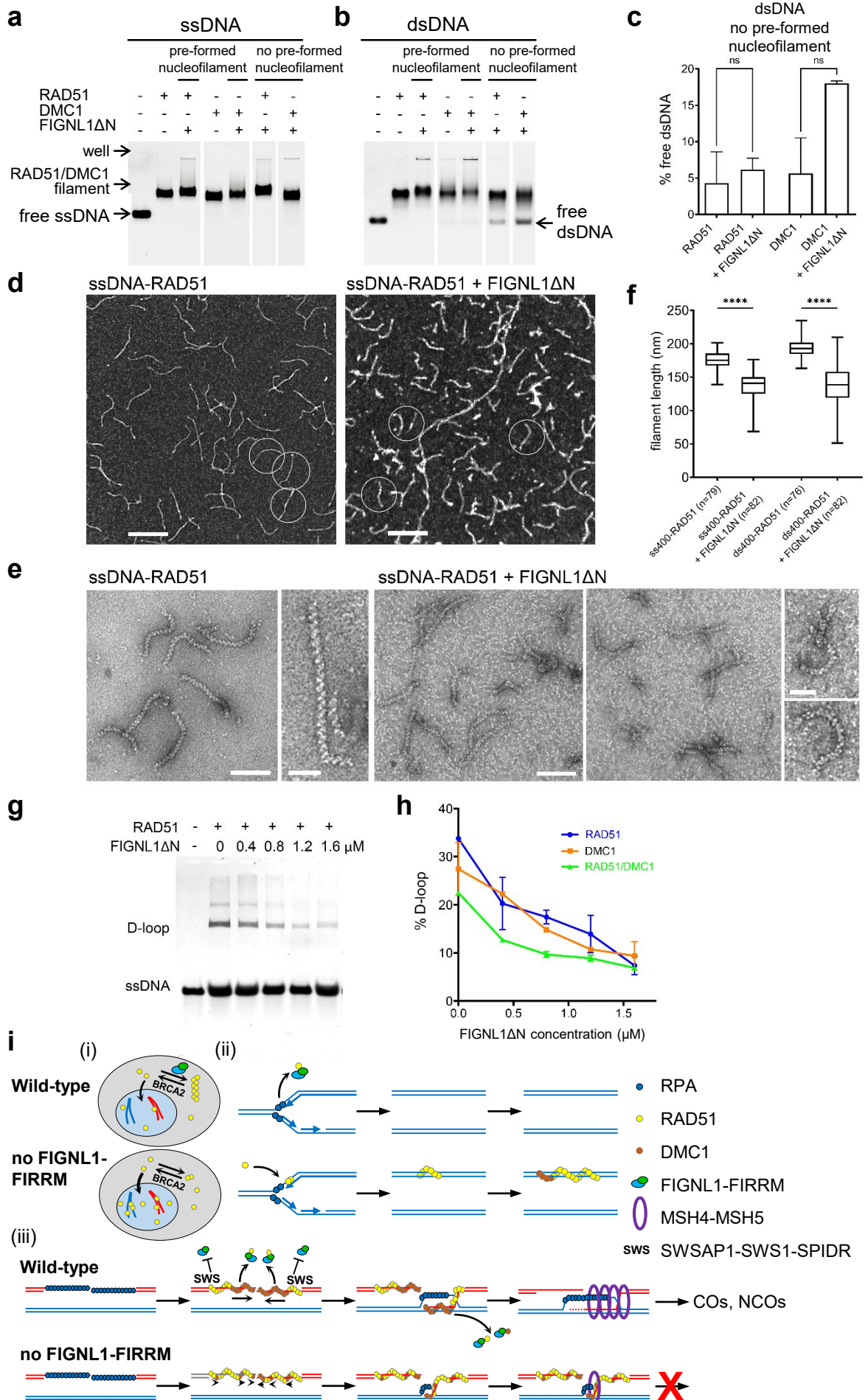
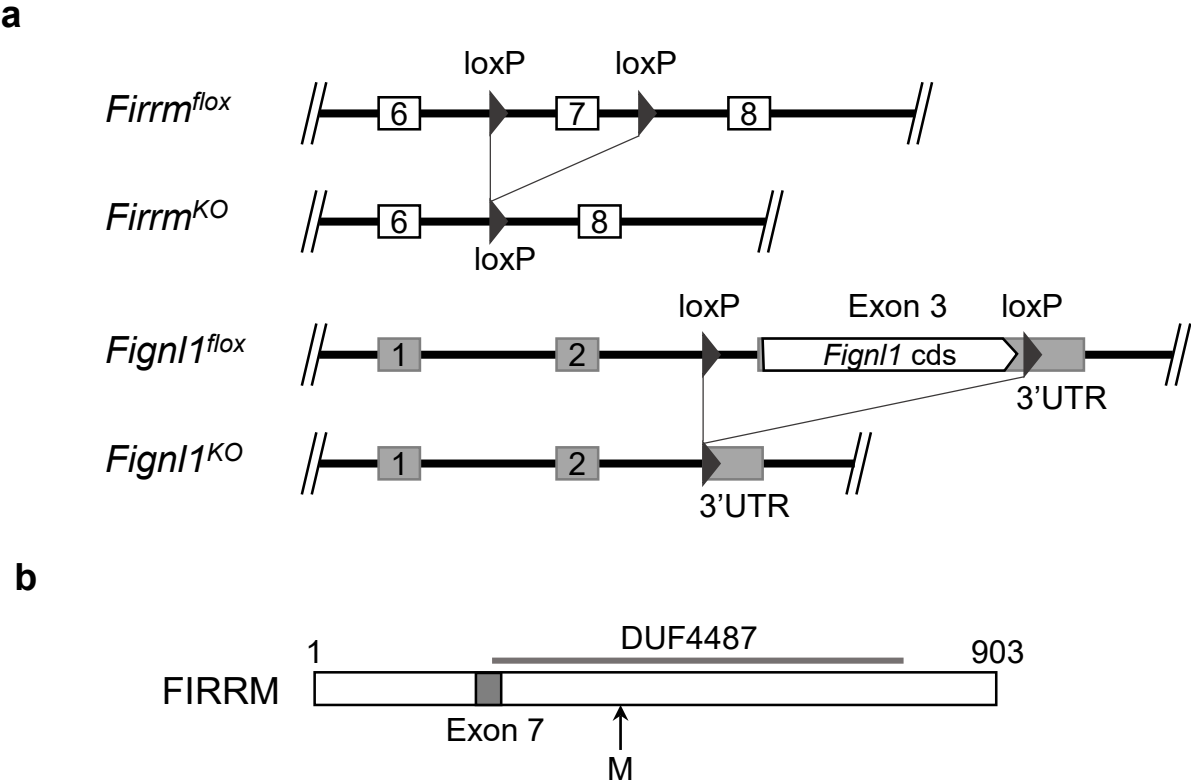


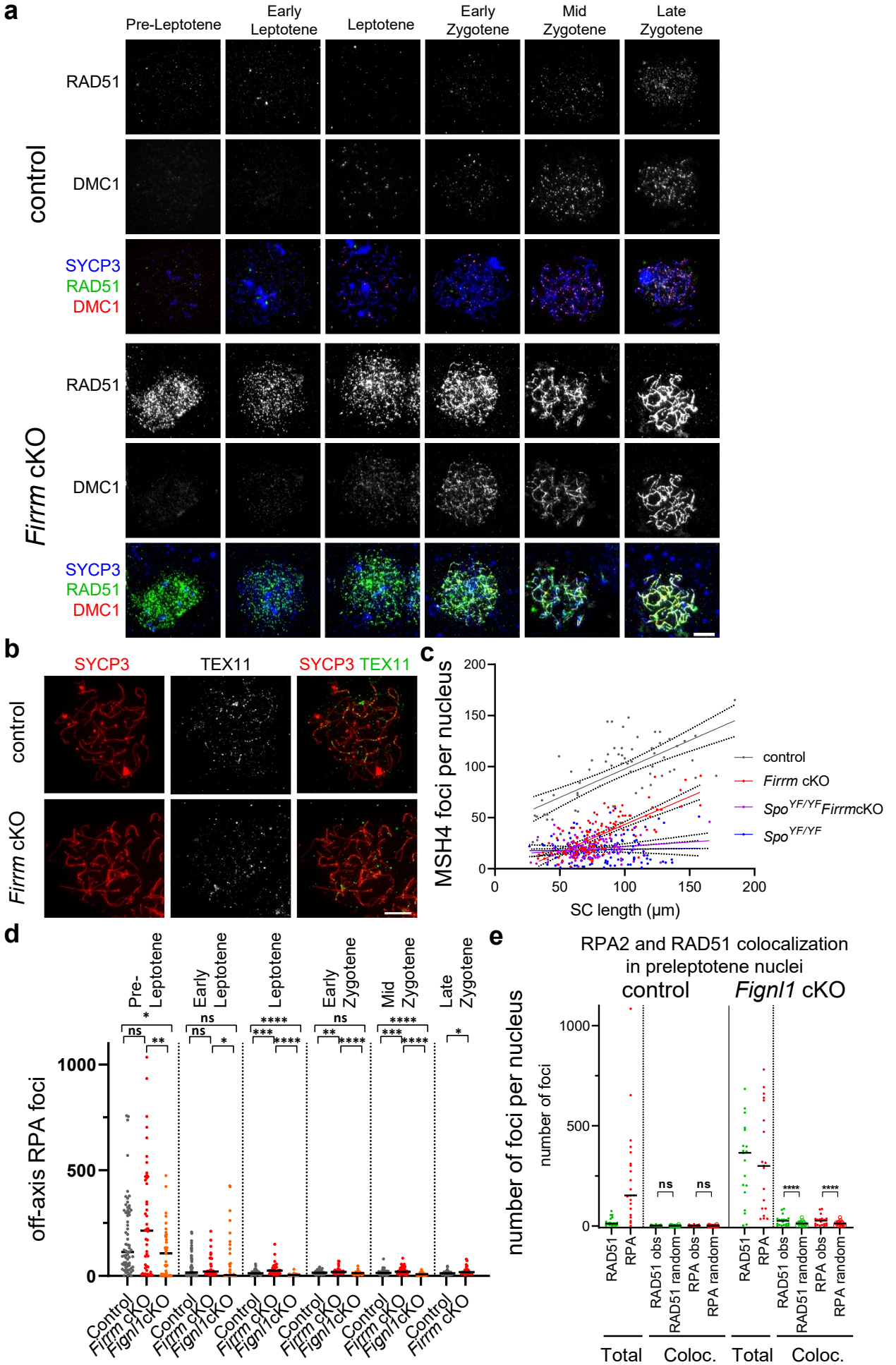
Figure 8



Extended Data Figure 1

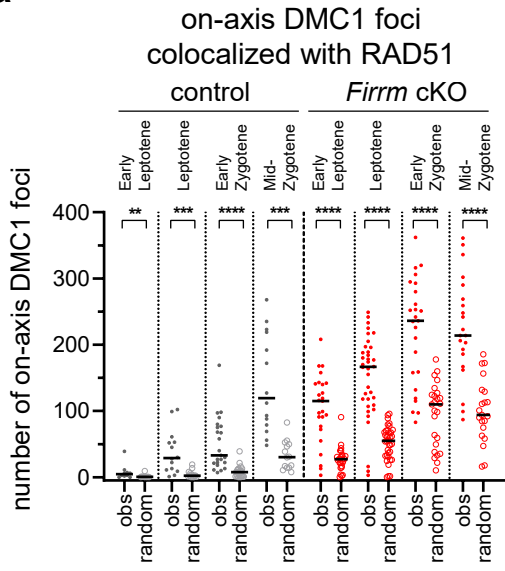


Extended Data Figure 2

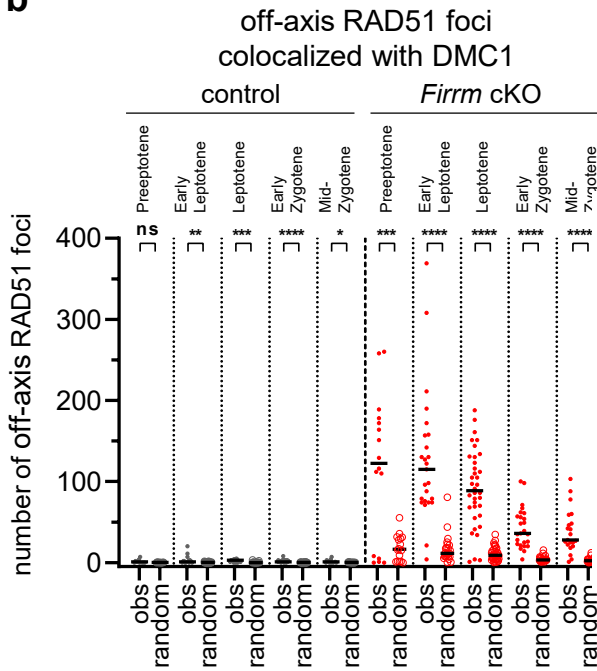


Extended Data Figure 3

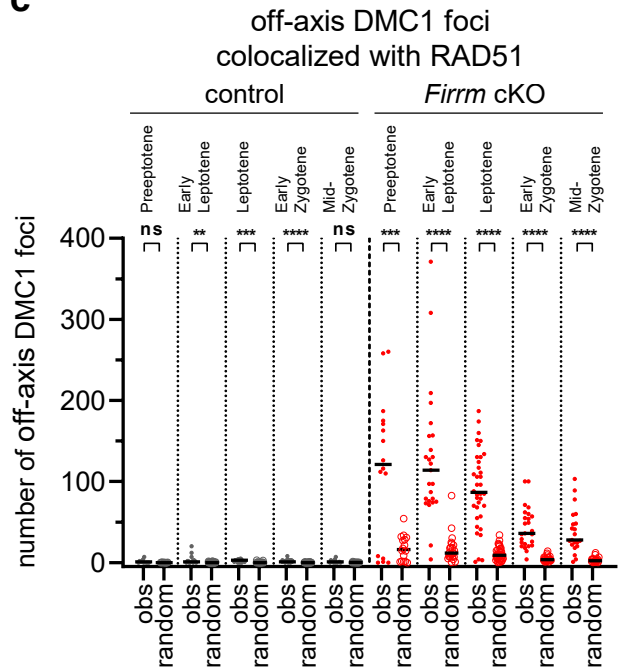
a



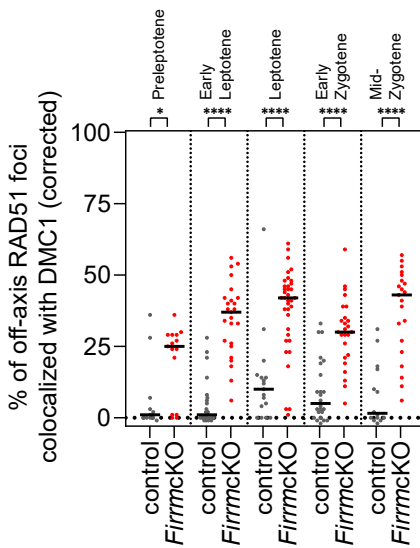
b



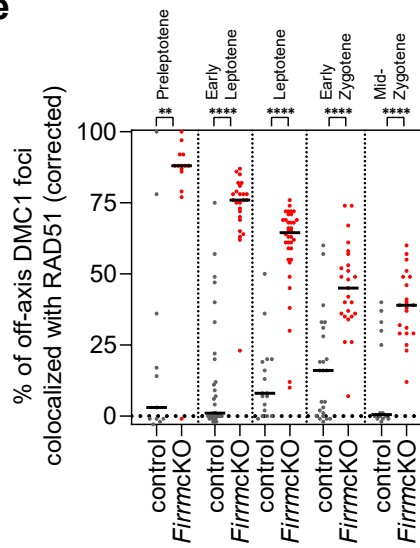
c



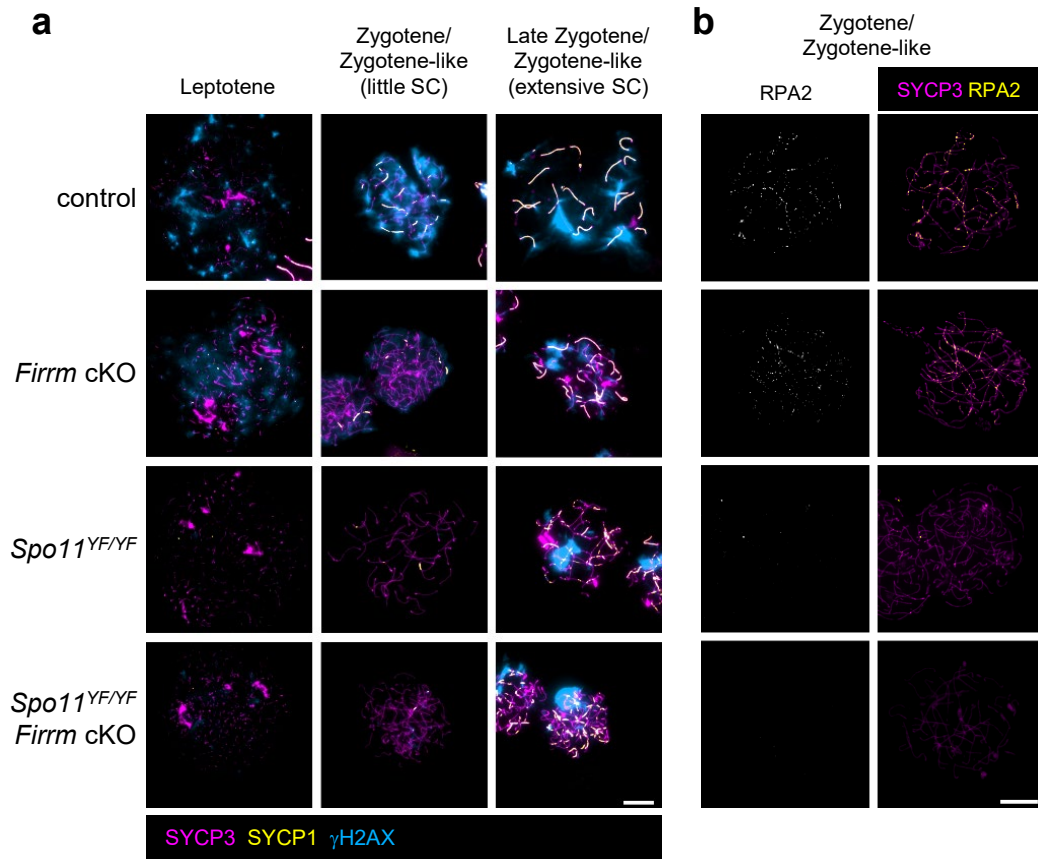
d



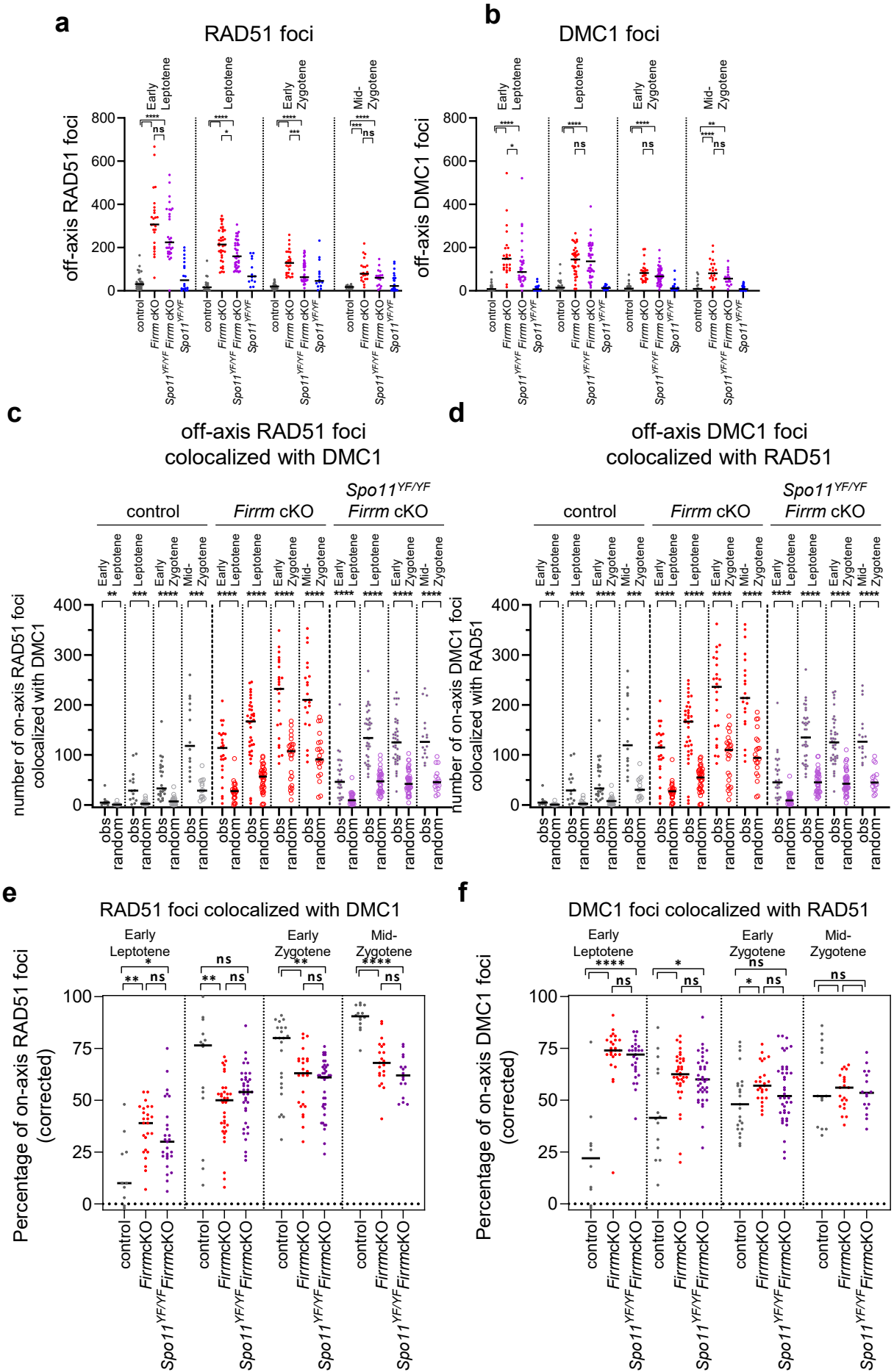
e



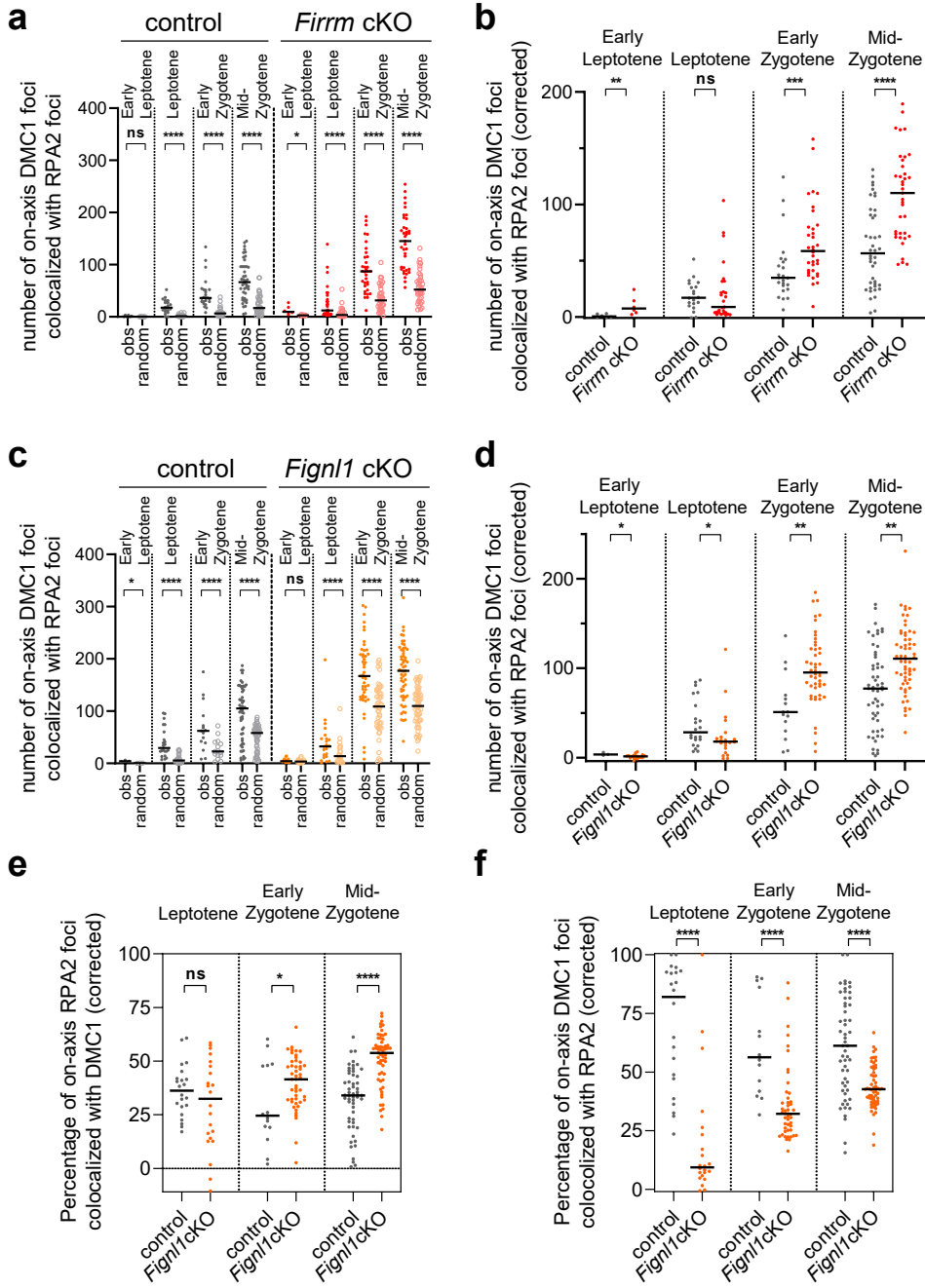
Extended Data Figure 4



Extended Data Figure 5

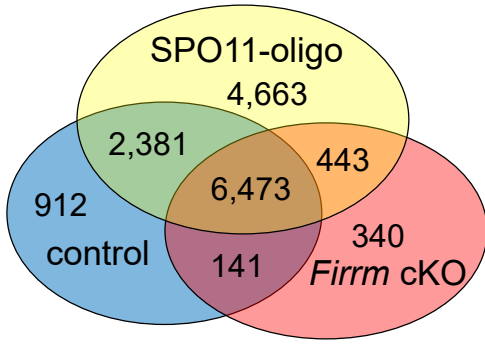


Extended Data Figure 6



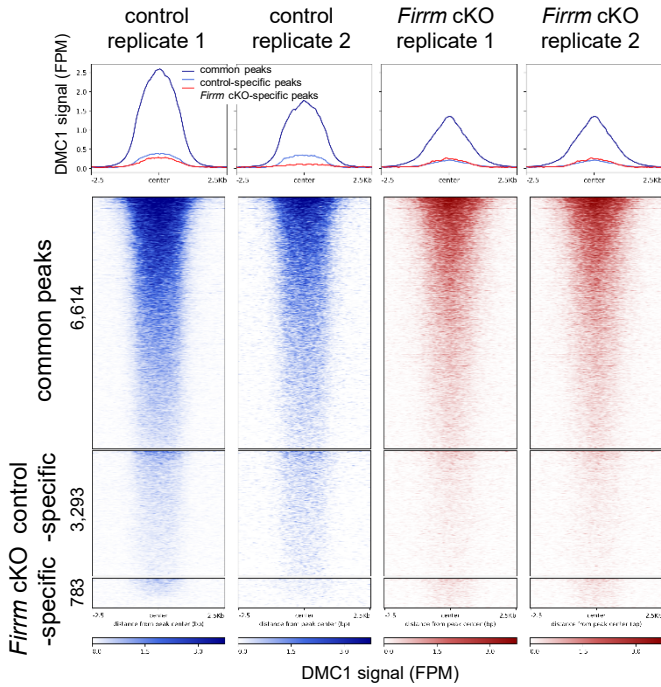
Extended Data Figure 7

a



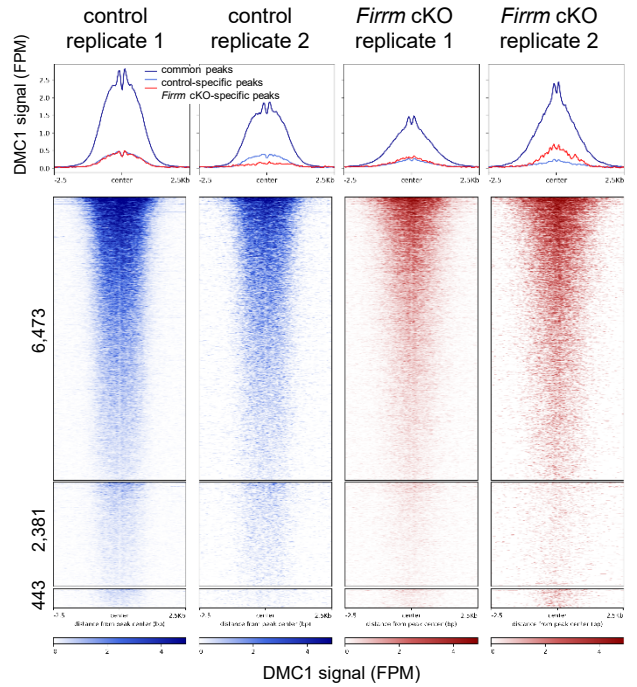
b

All peaks

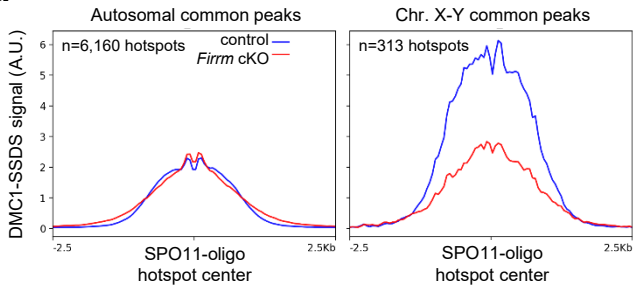


c

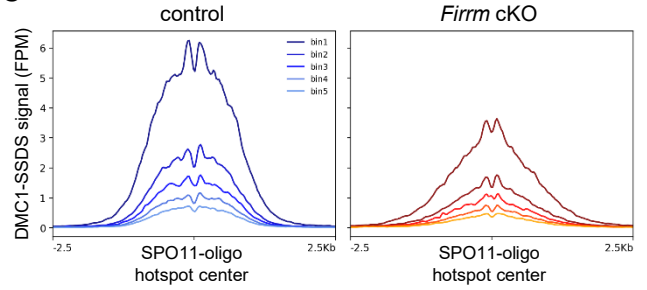
Peaks overlapping SPO11-oligo hotspots, centered to SPO11-oligo hotspot center



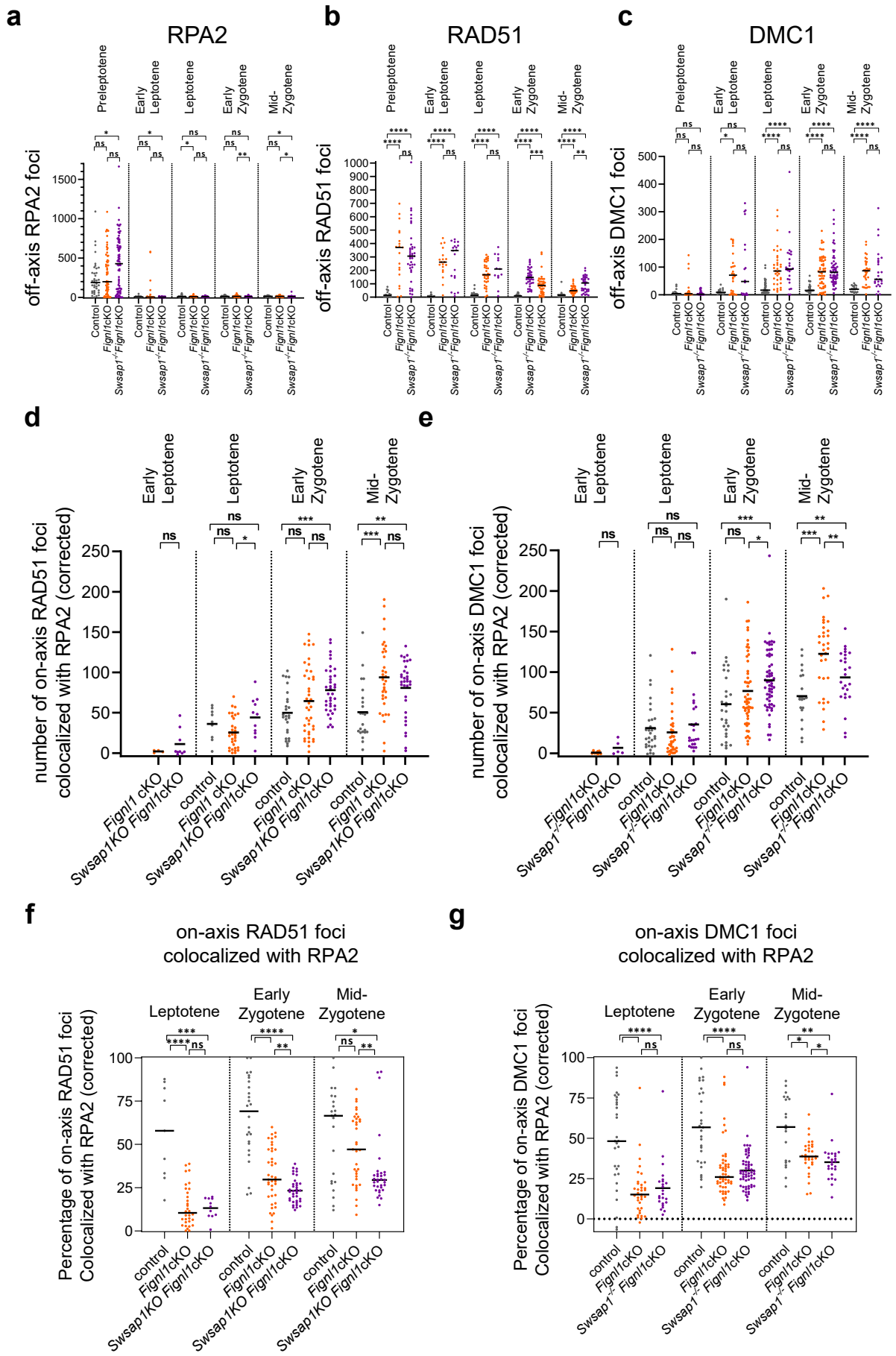
d



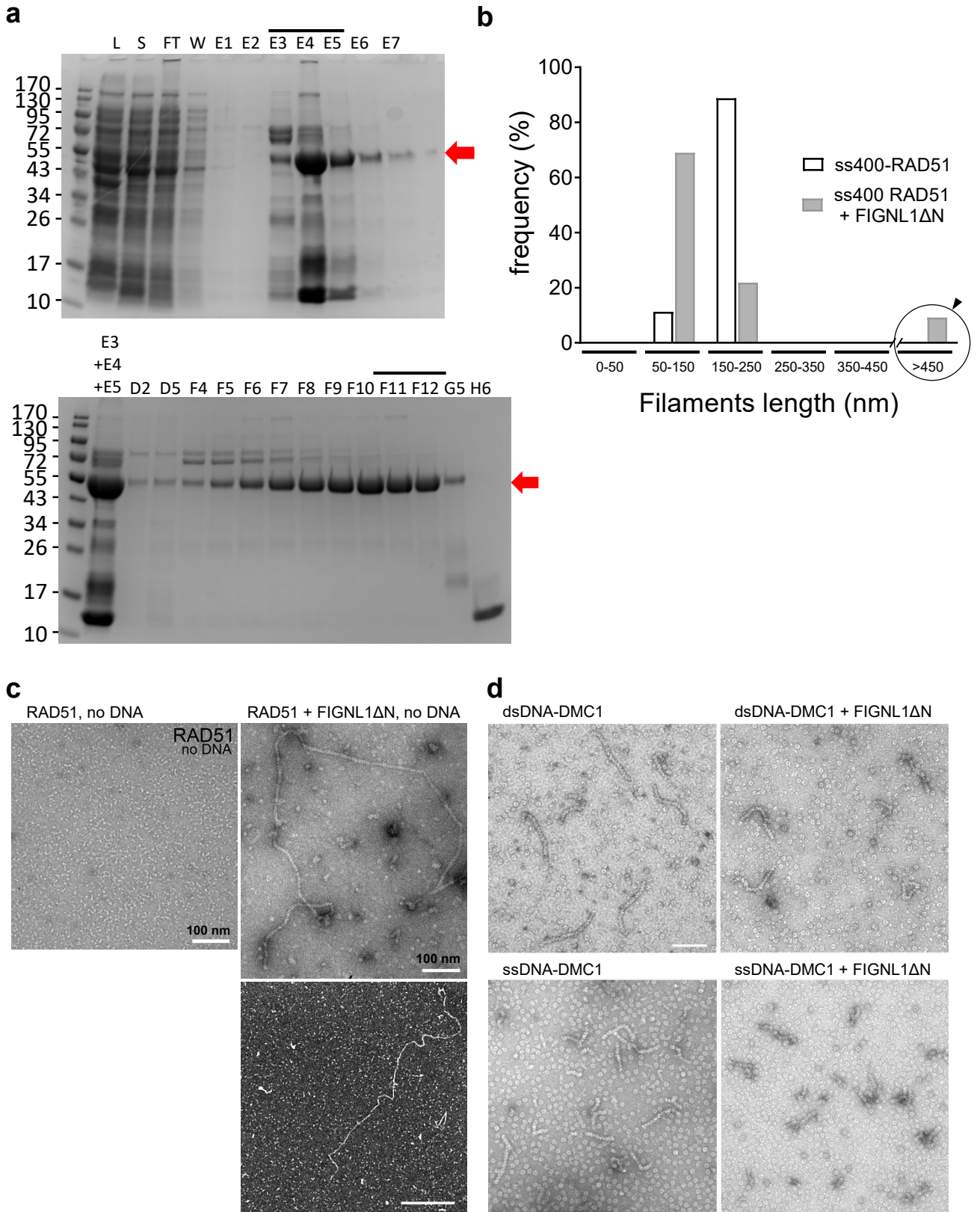
e



Extended Data Figure 8



Extended Data Figure 9



Source Data

